European Organisation for Nuclear Research

Department of Beams

Investigation into Possible Sources of Tune Jitter in the LHC

Imperial College London

École Polytechnique Fédéral de Lausanne

Department of Physics

Author:
Shriya Visavadia

Imperial ID:
01198026

Supervisor (CERN):
Dr. Rogelio Tomás Garcia

Supervisor (EPFL):
Dr. Tatiana Pieloni

July 1, 2019

1 Abstract

The beta function around an accelerator determines the shape and size of the beam. The LHC has demonstrated a beta function control to the 1% level [1]. However as its optics is pushed for increased performance, the measurement techniques are challenged by small perturbations. These measurements can be perturbed by tune jitters that find their origin in power supply ripples and the feed-down effect that stems from the machine's non-linearities and momentum changes. By extracting machine and orbit data and using accurate models, the effect of these perturbations in recent LHC optics measurements can be evaluated. The factors that contribute to these orbit jitters can also be investigated in order to search for methods to control them. It was found that the feed-down effect in sextupoles caused from orbit jitters is predicted to have a large effect on the tune shift. However the expected results are much more drastic than what is observed so other sources must be affecting the tune. One of the sources of orbit perturbation identified in this thesis is an unwanted activation of the orbit feedback system occurring simultaneously to an AC dipole kick data, potentially generating imprecise corrections.

2 Résumé

La fonction bêta autour de l'accélérateur établit la forme et la taille du faisceau. Le grand collisionneur de hadrons (LHC) a démontré un contrôle de la fonction bêta au niveau de 1% [1]. Cependant avec l'augmentation de la performance de l'optique, les petites perturbations posent des problèmes aux techniques de mesure. Ces mesures peuvent être perturbées par les sauts du ≪ tune ≫. Ces sauts prennent leur origine dans les ondulations de l'alimentation électrique et l'effet du ≪ feed-down ≫. Ceux-ci découlent des non-linéarités de la machine et le changement de la quantité de mouvement. Il est possible d'extraire les données d'orbite et de la machine et d'utiliser les modèles précis pour évaluer l'effet de ces perturbations en mesures optiques récentes du LHC. Nous pouvons également examiner les facteurs qui contribuent à ces sauts d'orbite pour chercher des méthodes qui peuvent les contrôler. Il a été démontré que l'effet du ≪ feed-down ≫ dans des sextuples, causé par les instabilités de l'orbite, a un impact important dans le changement de ≪ tunes ≫. Néanmoins, les résultats prévus sont plus drastiques que les résultats observés, ce qui nous permet de conclure que d'autres sources peuvent affecter l'orbite. Une source qui est identifié dans cette thèse est une activation indésirable du système de ≪ feedback ≫ en orbite. Cette activation s'est produite simultanément à un coup AC de dipôles, ce qui pourrait potentiellement provoquer des corrections imprécises.

3 Acknowledgements

There are many people I would like to give my utmost thanks to, as this thesis could not have existed without them. First I would like to thank Dr. Tatiana Pieloni for arranging this project and for sparking my interest in accelerators with her lecture series. To the beams department at CERN: Joschua, Tobias, Claudia and anyone else who provided helpful comments and advice along the way. I apologise for breaking Python not only once but in the weirdest ways. Also to Gavin Davies for being an excellent point of contact at Imperial and for answering my thousand questions about this thesis and more.

I would also like to give thanks to the friends and family who were extraordinarily supportive along the way: to my Mum and Dad for calming me through particularly stressful moments, for their dedicated support and for their wisdom. To all my friends for their kind, encouraging words and sense of humour.

Finally, I would like to express the greatest possible amount of gratitude to my incredible supervisor, Dr. Rogelio Tomás Garcia. This thesis was the result of his patient guidance, consistent dedication and insightful feedback. I would like to end this by quoting something that Rogelio would say, which was just in the context of realistic scientific result but I took to be much more profound:

In life, things are not linear.

Contents

4 Preface

The python scripts used functions to extract the initial orbit and tune data from PyTimber and to calculate the moving average of the tunes that were written for a thesis referenced as [2]. These functions were edited to perform the necessary tasks. All MADX scripts were developed and provided by the beams department at CERN and were again modified by the author to complete necessary tasks. All other scripts used for data analysis were written by the author of this thesis and the first instance of use of the functions previously mentioned are referenced when necessary in this thesis.

5 Motivation

The European Organisation for Nuclear Research (CERN) was established in 1954 by 12 founding countries located in Western Europe and has now expanded to include 23 member states and 8 associate member states around the world. The organisation was founded to develop scientific instruments powerful enough to investigate the most basic constituents of matter [3]. Many landmark achievements in particle physics have taken place at CERN such as the discovery of W and Z bosons in 1983 [4], the creation of antihydrogen atoms in 1995 [5] and the (probable) discovery of the Higgs Boson in 2012 using the Large Hadron Collider [6].

The Large Hadron Collider (LHC) is the largest and most powerful accelerator in the world and is the most recent addition to CERN's accelerator complex. This accelerator complex includes the LINAC 4 and the Proton and Super Proton Synchrotrons, which protons are gradually accelerated through before finally colliding at high energies of around 13-14 TeV [7] and a nominal luminosity of 10^{-34} cm^{-2} s^{-1} in one the 8 interaction regions of the LHC [8]. The 14 TeV maximum energy, and even luminosities double that of the nominal [9], that the LHC can currently reach was suitable to find the elusive Higgs boson but in order to discover new particles, accelerators that can improve on these numbers need to be built. Projects are already under way to try and achieve this such as the next upgrade of the LHC, the High Luminosity LHC (HL-LHC), also known as the HiLumi LHC, which will attempt to reach instantaneous luminosities which are a factor of 5 larger than the nominal value [10]. The Future Circular Collider (FCC) is another planned collider, hoping to push the frontiers of energy with an aim to reach collision energies of 100 TeV. The FCC will be the largest research facility, replacing the LHC and HL-LHC after they reach their discovery potential in 2035 [11].

The impressive size of the FCC with its 100 km circumference can be seen in Figure 1:

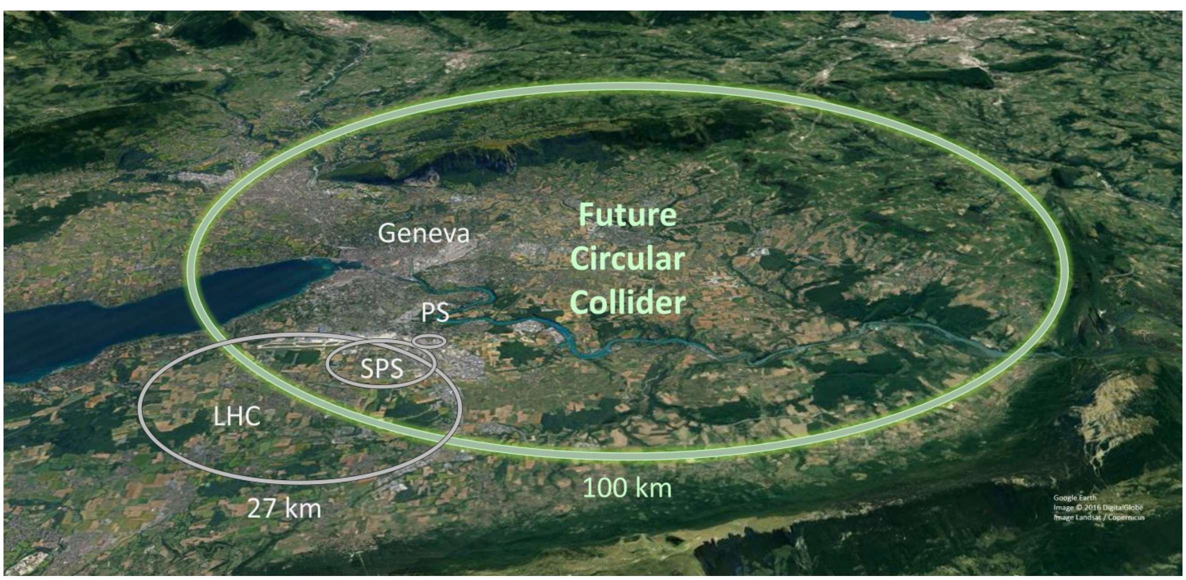

Figure 1: The planned Future Circular Collider in comparison with the LHC and other accelerators in CERN's accelerator complex.

Luminosity, L, is an important quantity in accelerator physics. The value is completely defined by accelerator and beam parameters. The interaction rate, R, is the number of particle interactions, or events, in a certain time. The luminosity is related to the interaction rate in the following way:

$$R = \frac{dN_p}{dt} = L \cdot \sigma(p) \ , \tag{1}$$

where N_p is the number of particles involved in a certain process and $\sigma(p)$ is the cross section for the process under study [12]. The cross section is an area that gives the probability that a collision event will take place. For rare events, like Higgs production, the cross section is much smaller as they are less likely [13]. Rare events like this are more likely to be observed when there is a high luminosity, which is why large experiments such as ATLAS and CMS occur at the nominal luminosity of 10^{-34} cm^{-2} s^{-1}.

Achieving maximum luminosity levels, thereby increasing the likelihood of particle collision [14] and the discovery of new phenomena, will require the LHC and future iterations of it to perform at its highest level. One of the ways in which an accelerator can reach these increased performance levels is by improving the stability of its beam. For luminosity, in particular, a controlled betatron function is imperative [15]. This is because accurate measurements of the β^* measurement, the value of the betatron function at the interaction point, is necessary for better luminosity control. The accuracy of this measurement can be greatly reduced by many and large amplitude jitters in the tune, which is the number of betatron oscillations per turn. It is therefore of great importance to investigate how to reduce these tune jitters to keep β^* measurements as accurate as possible for high luminosity control.

Tune jitters have their origins rooted in a variety of sources including orbit displacements. When the beam goes off-center in magnets of order N, they introduce an additional magnet component with an order of N-1. For example, sextupole magnets of order 2 introduce a quadrupole (order 1) component when misaligned. This phenomenon is called the feed-down effect [16]. This thesis will look particularly at the feed-down effect as a source of tune jitter, focusing on the misalignments of sextupole magnets.

Misalignments in magnet elements can significantly increase the errors on β^* measurements. It has been shown that errors will have an enhanced effect in the HL-LHC [15]. Therefore it is imperative that the accuracy of these β^* measurements be improved by controlling as many sources of error as possible so that the HL-LHC and future colliders are able to reach higher luminosities and the discoveries that come with this are unlocked.

6 Basics of Accelerator Physics

The beam of charged particles is influenced by different types of magnets as it travels around the accelerator. As the trajectory of the particles is curved, the particles must experience a bending force, which is provided by a dipolar magnetic field. In practice, the beam will deviate from the ideal orbit and will need to be regularly focused to keep it as close to the design orbit as possible. Quadrupolar magnetic fields provide these focusing forces.

6.1 Lorentz Force

Since the particles are charged, they will feel a force from the electric fields as well as the magnetic ones. The equation of motion of these charged particles experiencing both an electric and magnetic field is governed by the Lorentz force :

$$\frac{d^2\vec{r}}{dt^2} = \vec{F}_L = q \cdot (\vec{E} + \vec{v} \times \vec{B}); \qquad \vec{r} = \begin{pmatrix} x \\ y \\ z \end{pmatrix}; \quad \vec{v} = \frac{d\vec{r}}{dt}\,, \tag{2}$$

where q is the particle charge, '$\times$' denotes the vector product and $\vec{r}$, $\vec{v}$, $\vec{E}$ and $\vec{B}$ are the vector presentations of the particle position, velocity and the electric and magnetic fields in the storage ring, respectively [17].

6.2 Frenet-Serret Coordinate System

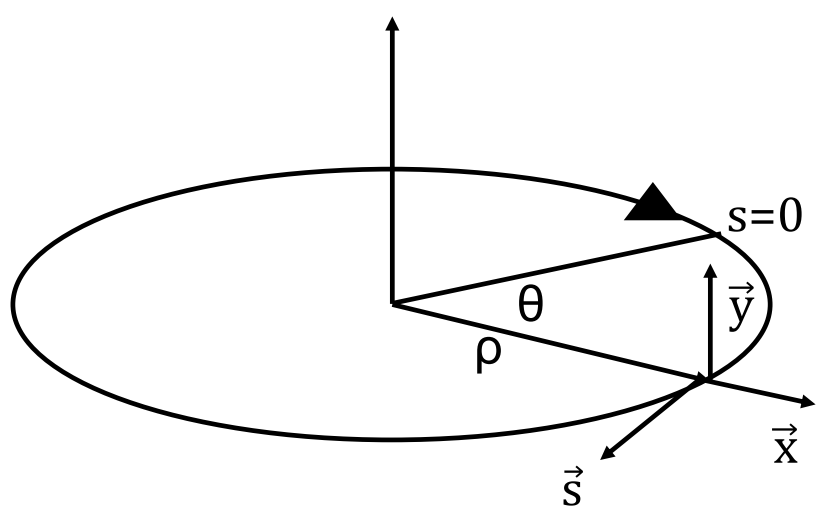

Figure 2: The curvilinear Frenet-Serret coordinate system used to describe in particle motion in accelerators.

The coordinate system used in accelerator physics is the Frenet-Serret, or curvilinear, reference system. As can be seen in Figure 2 it is a right handed orthogonal system with coordinates x, y and s shown relative to an ideal, closed orbit. The x and y vectors refer to the horizontal and vertical positions of the particle at a particular s location. The s vector refers to the tangential position of the particle relative to the particle's orbit. The radius is shown by ρ and the angle traversed between $s = 0$ and s is θ.

6.3 Closed Orbit

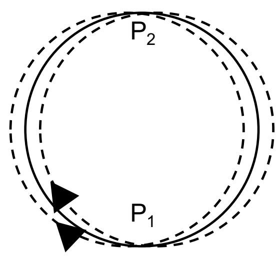

Figure 3: A figure

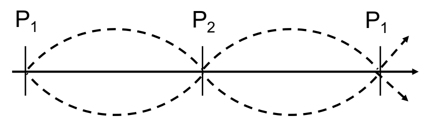

Figure 4: In a homogeneous magnetic field all particles that arrive at P_1, deviated from the design orbit, move on circles with the same radius before meeting again at P_2. This looks as if the trajectory is being focused to the design orbit, which can be seen more clearly in the figure on the right, which shows the same case but from within the rotating coordinate system.

The closed orbit of the design orbit is a perfect circle with radius, ρ. If the particle motion is stable then any deviations of the particle from the design orbit will incur orbit restoring forces that lead to oscillations around the orbit. These oscillations are called betatron oscillations. This occurs in the homogeneous field of the dipole, where particles that diverge from the ideal orbit will meet again after a 180° revolution [18] as can be visualised with Figure 4. It is important to note that this situation is for an accelerator with a homogeneous dipolar field. For a synchrotron, the type of accelerator that the LHC is, this closed orbit is more complex due to strong focusing effects from quadrupoles.

6.4 Dipoles

Dipoles, or bending magnets, are multipole magnets of order 1, which are used to deflect the beam so that it travels in a circle following the ideal orbit as closely as possible. It weakly focuses the orbit. Normal dipoles are used for horizontal bending while skew dipoles are for vertical bending. The dipole magnetic field is homogeneous so its value in the x and y planes are constant [18].

6.4.1 Cyclotron Equation

The Lorentz force acts as a centripetal force in a uniform dipole field. By equalising the forces and solving for the equilibrium radius of curvature, ρ, the cyclotron equation can be found:

$$\rho = \frac{p}{e \cdot B_0} \; . \tag{3}$$

Here p is the particle's momentum, e is its charge and B_0 is the uniform dipole field.

6.4.2 Beam rigidity

The product, ρB_0, is called the beam rigidity and it can be expressed by rewriting Eq. 3 in practical units:

$$[T \cdot m] B\rho = \frac{1}{0.29979} p \left[\frac{GeV}{c} \right] . \tag{4}$$

6.4.3 Dipole strength

The normalised dipole strength is defined as the inverse of the radius of curvature:

$$k_0 = \frac{1}{\rho} = 0.29979 \frac{B[T]}{p[GeV/c]} , \tag{5}$$

where the dipole strength, k_0, is given in units of m^{-1}.

6.5 Quadrupoles

Quadrupoles are multipole magnets of order 2 that have 4 poles with a hyperbolic contour. Therefore they focus in one plane (say, horizontally) and defocus in the other (vertically). The sign of the gradient, g, determines which planes will have focusing or defocusing. A change in current direction, particle charge or direction of motion will change the focusing so that the quadrupole focuses in the vertical plane and defocuses in the horizontal [18].

6.5.1 Quadrupole magnetic field

While dipole fields are uniform, quadrupoles are linearly dependent on the deviation from the magnet's axis so the magnetic field experienced by a particle traversing the quadrupole is given by:

$$B_x(x, y) = +g \cdot y , \tag{6}$$

$$B_y(x, y) = +g \cdot x , \tag{7}$$

where x and y are the horizontal and vertical axis deviations, respectively, and the gradient, g, is defined as:

$$g = \frac{\partial B_y}{\partial x} . \tag{8}$$

6.5.2 Quadrupole strength

The normalised quadrupole strength is analogous to the normalised dipole strength and in units of m^{-2} can be written as:

$$k_1 = \frac{qg}{p} = 0.29979 \frac{g[T/m]}{p[GeV/c]} \ . \tag{9}$$

6.5.3 Strong Focusing

For a positive gradient, the horizontal force acting on the particles makes the motion stable in the horizontal plane, like in the case of the dipole field. However the vertical force acting on particle deflects the particles away from the ideal orbit, causing particle motion in this plane to be unstable in the vertical plane. In order for the particle motion to be focused overall in both transverse planes, an alternating sequence of quadrupole polarities is necessary. This is the strong focusing method [17]. A FODO cell is a combination of focusing and defocusing magnets that acts upon the beam to give this overall focusing effect. FODO cells are discussed in more detail in section 8.1.

6.6 Sextupoles

A sextupole is a multipole magnet of order 3 that is used to correct 'chromatic' error. (See section 7.3).

6.6.1 Sextupole magnetic field

Sextupoles generate a nonlinear field that can be parameterised as:

$$B_x = g' \cdot x \cdot y \ , \tag{10}$$

$$B_y = \frac{1}{2} \cdot g' \cdot \left(x^2 - y^2\right) \ , \tag{11}$$

where the gradient g' is a function of the current through the magnet coils.

6.6.2 Sextupole strength

The normalised strength of a sextupole is defined with units of m^{-3} as

$$k_2 = \frac{e \cdot g'}{p} = 0.29979 \cdot \frac{g'\left[T/m^2\right]}{p[GeV]} \ . \tag{12}$$

6.7 Particle Equation of Motion in Magnets

6.7.1 Hill's Equation

If we assume that the horizontal and vertical planes are not coupled, we can define the particle equation of motion in one of the planes (say, horizontal) using Hill's equation. Hill's equation is essentially the equation of motion of a simple harmonic oscillator but with a non-constant coefficient K [19] so it can be expressed as

$$x'' + K(s)x = \frac{1}{\rho} \cdot \frac{\Delta p}{p} \,, \tag{13}$$

where $K(s)$ is periodic so that $K(s) = K(s+L)$, L is the circumference of the design orbit and $\frac{\Delta p}{p}$ is the relative momentum deviation. The value of $K(s)$ depends on the magnet that the particle is passing through is defined for drift space (an area with no magnets), dipoles and quadrupoles [17] with the following:

$$K(s) = \begin{cases} 0 & \text{drift space} \\ \frac{1}{\rho^2} & \text{dipole field} \\ k_1 & \text{quadrupole field} \end{cases} \,. \tag{14}$$

6.7.2 Floquet Theorem

Floquet's theorem states that the solutions to the Hill's equation with non-constant $K(s)$ can be written in terms of sine and cosine functions [17, 20]. The independent solutions for $x(s)$ are as follows:

$$\begin{aligned} x(s) &= \sqrt{A} \cdot \sqrt{\beta(s)} \cdot \sin\left(\phi(s) - \phi_0\right), \\ x(s) &= \sqrt{A} \cdot \sqrt{\beta(s)} \cdot \cos\left(\phi(s) - \phi_0\right) \;. \end{aligned} \tag{15}$$

Here A is an arbitrary constant and the amplitude, $\beta(s)$, and phase, $\phi(s)$, terms, are modulated with the s coordinate and are discussed further in the following section.

6.8 Beta Function & Tune

6.8.1 Beta Function

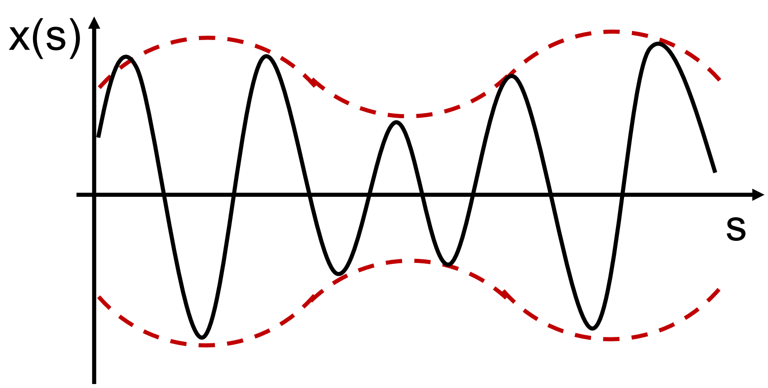

Figure 5: A visual representation of the solutions to Hill's equations as stated in Eq. 15. The s dependent amplitude, the β function, is shown here by the dashed red line. The particle motion $x(s)$ is shown in black.

The optical beta function (β function) is the amplitude term that is dependent on s. The β function, which is the amplitude of the solution, can be seen as the red dashed line enclosing the particle motion in Figure 5.

By substituting the solutions (Eq. 15) into Hill's equation (Eq. 13), we get the following non-linear differential equation for the β function:

$$\frac{1}{2} \cdot \beta(s) \cdot \beta''(s) - \frac{1}{4} \cdot \beta'^2(s) + K(s) \cdot \beta^2(s) = 1 \ . \tag{16}$$

The relationship between the β function and a constant coefficient $K(s)$ is then:

$$K(s) \cdot \beta^2(s) = 1 \rightarrow \beta = \frac{1}{\sqrt{K}} \ . \tag{17}$$

Eqs. 16 and 17 state that for weak focusing, where $K(s)$ is small, the accelerator has large beta functions.

6.8.2 Phase Advance

The phase advance, which is modulated in s, is also a function of β. It is defined as [17]:

$$\phi(s) = \int_{s_0}^{s} \frac{dt}{\beta(t)} \tag{18}$$

6.8.3 Tune

The tune, or Q, value is the number of betatron oscillations per turn. It can be defined in terms of the phase advance and there in terms of β:

$$Q = \frac{1}{2\pi}\phi(s) = \frac{1}{2\pi} \oint \frac{dt}{\beta(t)} \ . \tag{19}$$

6.9 Twiss Parameters & the Transfer Matrix

The β function is one of 3 Twiss (or Courant-Snyder) parameters (α, β & γ). They completely define the machine's optics and are a periodic function of s. The following relationship exists between the 3 parameters [18]:

$$\alpha(s) = -\frac{1}{2}\frac{d\beta}{ds}(s) \ \text{ and } \ \gamma(s) = \frac{1 + \alpha(s)^2}{\beta(s)} \ . \tag{20}$$

It is useful to define a transformation matrix that can propagate any initial conditions of a trajectory to another s coordinate. By defining this transformation matrix over one revolution and in terms of the Twiss parameters, we get the unperturbed 'one-turn map'. The conditions for this require setting s equal to $s_0 + L$ so that $\Delta\phi = 2\pi Q$. We therefore obtain:

$$\underline{\Phi}\left(s_0, s_0 + L\right) = \begin{pmatrix} 1 & 0 \\ 0 & 1 \end{pmatrix} \cdot \cos(2\pi Q) + \begin{pmatrix} \alpha\left(s_0\right) & \beta\left(s_0\right) \\ -\gamma\left(s_0\right) & -\alpha\left(s_0\right) \end{pmatrix} \cdot \sin(2\pi Q) \ . \tag{21}$$

The Trace of the map, which is useful for calculating the tune shift, is given by:

$$\mathrm{Tr}\left(\underline{\Phi}\left(s_0, s_0 + L\right)\right) = 2 \cdot \cos(2\pi Q) \ . \tag{22}$$

7 Error Theory

7.1 Overview of Magnet Perturbations

The three main sources of perturbations in both dipole fields and quadrupole fields are field error settings, energy errors of particles in the accelerator and feed-down errors [17]. These will be briefly described in the remainder of this section. Perturbations in magnets have different effects depending on what order the magnet has.

7.1.1 Dipole Perturbations

Dipole perturbations lead to a change in the closed orbit of the accelerator. These can have a serious impact on the machine performance including:

- beam lifetime reduction
- change of beam energy
- coupling of horizontal and vertical motion [21, 17].

The dipole perturbation term that comes from errors in the dipole field settings is of the form:

$$\Delta k_0 = \frac{q \cdot \Delta B}{p} \ . \tag{23}$$

The amount of deflection that particles in a dipole field experience depends on their energy. Therefore a detour from the design beam energy will result in a deflection angle and closed orbit error. This energy deviation leads to a dispersive orbit.

7.1.2 Quadrupole Perturbations

The quadrupole field settings generate a perturbation term defined as:

$$\Delta k_1 = \frac{q \cdot \Delta g}{p} \; . \tag{24}$$

These additional field components generate extra focusing terms which can have a major effect on the beta functions and tune. Some of the consequences of this include:

- resonances in particle motion from tune errors
- beam size increase from changes in the beta function oscillation amplitudes.

7.2 Feed-Down Effect

The feed-down effect occurs when a misaligned magnet of order N generates a magnetic field of order N-1 [16]. We shall focus on the case of normal sextupoles which generate quadrupolar components when misaligned.

7.2.1 Misaligned Sextupole Magnetic Field

For a sextupole that is horizontally misaligned by an amount dx, Eqs. 10 and 11 for the sextupole magnetic field change so that x now encompasses this offset with respect to the ideal design orbit:

$$B_x = g' \cdot (x + dx) \cdot y \; , \tag{25}$$

$$B_y = \frac{1}{2} \cdot g' \cdot \left([x + dx]^2 - y^2 \right) \; . \tag{26}$$

By expanding, the new equations for the sextupole magnetic field can be written as:

$$B_x = g' \cdot x \cdot y + g' \cdot dx \cdot y \; , \tag{27}$$

$$B_x = \frac{1}{2} \cdot g' \cdot \left(x^2 - y^2 \right) + \quad g' \cdot dx \cdot x + \frac{1}{2} \cdot g' \cdot dx^2 \; . \tag{28}$$

By comparing these to Eqs. 6 and 7 for the quadrupole magnetic field, we can see that Eqs. 27 and 28 now have an additional quadrupole term with an effective gradient $g = g' \cdot dx$ and an effective normalised quadrupole strength of [17]:

$$\Delta k_1 = k_2 \cdot dx \; . \tag{29}$$

This means that the misaligned sextupole will give a quadrupolar kick that will consequently affect the tune to possibly cause tune jumps and jitters [16].

7.2.2 Tune Shift due to Field Errors

The unperturbed one turn map is given by Eq. 21. We can consider the additional quadrupole component from the misaligned sextupole to be a thin quadrupole element with strength k_1. Its transfer matrix is then represented by:

$$\underline{m} = \begin{pmatrix} 1 & 0 \\ -\Delta k_1 ds & 1 \end{pmatrix} . \tag{30}$$

By using Eq. 22 which links the trace and the tune, we can get an expression for the tune shift caused by the misaligned sextupole:

$$\Delta Q = \frac{1}{4\pi} \cdot \beta_0 \left(s_0\right) \cdot \Delta k_1 \left(s_0\right) ds . \tag{31}$$

The total tune shift can be found by integrating over the s coordinate:

$$\Delta Q = \frac{1}{4\pi} \oint \beta_0(s) \cdot \Delta k_1(s) ds . \tag{32}$$

If this is integrated over the whole accelerator, the integral over s is just equal to the accelerator circumference, L. The additional quadrupole component's strength, k_1, can be defined in terms of the sextupole strength as shown in Eq. 29. By applying the above statements, Eq. 32 can be rewritten to give the total tune shift from the misaligned sextupole. For the horizontal direction this is given by Eq. 33:

$$\Delta Q_x = \frac{1}{4\pi} \cdot k_2 L \cdot dx \cdot \beta_x , \tag{33}$$

where k_2 is the misaligned sextupole's strength, β_x is the horizontal beta function and dx is the sextupole misalignment.

7.2.3 MADX simulation

Eq. 33 can be visualised in red in Figure 6. A selected sextupole, with a known normalised strength and horizontal beta amplitude function, was chosen and misaligned from -5 mm to 5 mm. Simulations in the CERN particle accelerator simulator program MADX, were also run for the same sextupole to compare the results for tune shift versus orbit misalignment in theory and in MADX simulations. There was some non-linearity in the tune shifts measured with MADX, which is to be expected since perfect linearity can only be expected in theory. Figure 6 was plotted to show that, despite some non-linearity, there is good agreement between the theoretical prediction of tune shift with orbit alignment and the real tune shift measured by MADX.

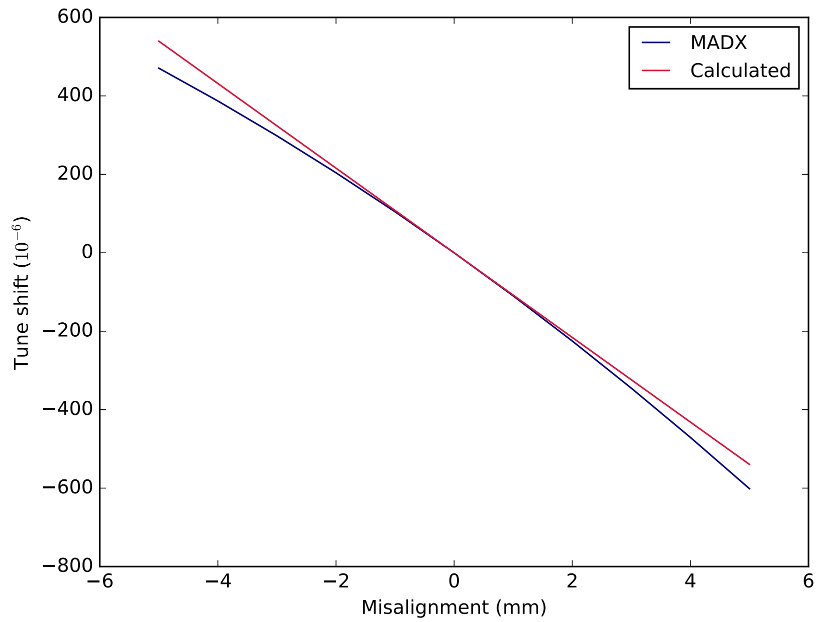

Figure 6: This graph represents Eq. 33 and shows simulations in MADX for the tune shift varying with hoirzontal misalignments in a sextupole from -5 mm to 5 mm.

7.3 Chromaticity

From Eqs. 9 (strength for an on-momentum particle) and 24 (strength for an off-momentum particle), we can see that the quadrupole strength, and therefore its focusing, is dependent on the particle momentum [17]. This momentum dependence of the focusing, which, in turn, causes tune changes,is called a chromatic effect [19]. The variation of the betatron tune, Q, with the relative momentum deviation is called chromaticity. The relative momentum deviation, δ and the definition of chromaticity are given below [22]:

$$\delta = \frac{\Delta p}{p} \, , \tag{34}$$

$$Q' = \frac{dQ}{d\delta} \, , \tag{35}$$

The tune shift can be defined:

$$\Delta Q = Q' \frac{\Delta p}{p} \, . \tag{36}$$

Q' is called the natural chromaticity and is the chromaticity due only to the linear elements of the lattice, i.e.: dipoles and quadrupoles - not sextupoles [22]. It is important to note that if sextupoles were being considered, Q' would just be the chromaticity. The lattice is just the magnet structure of the accelerator. By equating the tune shift of Eq. 36 to the tune shift due to a quadrupole gradient error, we get an expression for the natural chromaticity [23], which is the result in square brackets in Eq. 37.

$$\Delta Q = \frac{1}{4\pi} \int \beta(s) \Delta k(s) ds = \left[\frac{1}{4\pi} \int \beta(s) k(s) ds \right] \frac{\Delta p}{p} \ . \tag{37}$$

Chromaticity corrections are discussed in section 8.1.3.

7.3.1 Momentum deviation and orbit displacement

The horizontal orbit displacement at a specified s location, $dx(s)$, can be related to the momentum deviation by multiplying by the dispersion function at the same s:

$$dx(s) = D(s) \cdot \delta \ . \tag{38}$$

The dispersion function, $D(s)$, gives the dispersion orbit position at a certain s location. Particles with a beam energy deviated from the design beam energy pass through dipoles and are deflected, changing the closed orbit. This change in closed orbit is the dispersion orbit.

For a ring average orbit misalignment $\langle dx \rangle$ and an average dispersion orbit $\langle D_x \rangle$, the following relation can be made with the tune shift in Eq. 36:

$$\Delta Q = Q' \frac{\delta p}{p} = Q' \frac{\langle dx \rangle}{\langle D_x \rangle} \ . \tag{39}$$

7.4 AC Dipole Kicks

AC dipole kicks are used as an excitation that induces large transverse displacements in the beam. They are used to study properties of the LHC lattice that require the beam to be deviated to large displacements with respect to the design orbit. We can think of the tune, the number of betatron oscillations per turn, as a natural frequency of the transverse beam. Therefore, if the tune is at an integer or half-integer value, resonance effects will take place and the transverse oscillation amplitudes will become very large. The AC dipole method uses this principle of the beam responding significantly to excitations at frequencies close to integer or half-integer values of the tune [24].

8 Orbit Correction

8.1 LHC FODO cell

This section explains how the LHC's FODO cells are set up with elements that can correct the orbit after a displacement from the closed design orbit. Figure 7 shows the schematic layout of a simplified version of the LHC's FODO cell [25]. It has been simplified to exclude some elements that will not be relevant in the context of this thesis.

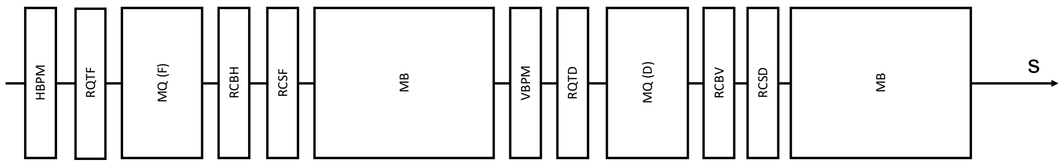

Figure 7: This shows a simplified schematic layout of the LHC's FODO cell. Each quadrupole has a BPM and optical, orbit & sextupole correctors. A simplified version of the dipole layout is presented here with further explanation in section 8.1.1

8.1.1 MQ & MB

The FODO in FODO cell refers to the layout of the cell with a Focusing quadrupole, dipole magnets for Orbit guidance, a Defocusing quadrupole and dipole magnets again. The MQ elements in Figure 7 represent the Main Quadrupoles which can be focusing (F) or defocusing (D).

The MB elements represent dipoles. In actuality, there are 3 dipole magnets within the MB area in Figure 7. The 3 dipole magnets are either A dipoles (MBA) or B dipoles (MBB). There are corrector elements on each side of the dipole depending on which type of dipole it is [25].

8.1.2 BPMs

Beam Position Monitors (BPMs) are used to measure the closed orbit position. BPMs measure the orbit position by processing data that is collected from pick-up electrodes in the beam pipe. One of the most common types of pick-up electrode is the electrostatic (or capacitive) pick-up. Here, as the beam passes, it induces electric charges in the electrodes where more are induced on the side closer to the beam. From the difference in the induced charge, the beam position can be inferred [26].

Since misalignments in quadrupoles are the most common reason for closed orbit distortions, BPMs are positioned near orbit correctors and quadrupoles to allow for local correction and a more accurate orbit position reading. Horizontal BPMs (HBPM) are placed near focusing quadrupoles and vertical BPMs (VBPM) are near defocusing quadrupoles [17].

8.1.3 RQT, RCB & RCS

RQTF and RQTD correctors are placed next to focusing and defocusing quadrupoles, respectively. These are optical correctors called tune-shift or tune quadrupoles, which are used to induce tune shifts and therefore can have a direct effect on the tune.

RCBH and RCBV corrector are horizontal and vertical orbit corrector magnets that are installed at focusing and defocusing quadrupoles, respectively. They are used to kick the orbit back the reference orbit.

RCSF and RCSD sextupoles, also called MS sextupoles, are used to correct chromaticity and are placed at focusing or defocusing quadrupoles, respectively. Sextupoles are added into the accelerator's lattice to correct the natural chromaticity produced by the dipoles and quadrupoles. When a charged particle that is travelling off center passes through a sextupole, it receives a kick that is proportional to its displacement from the axis centre.

8.2 Orbit Feedback System

The LHC Orbit Feedback system works by first reading beam position data from BPMs. This BPM data is then compared to a reference orbit and corrected in space and time. The correction in space is detailed in section 8.3. The new deflection angles calculated by the correction are converted into currents and these new settings are sent to Power Converter (PC) gateways to change the current in various orbit correctors [27]. These include the RCBH and RCBV orbit corrector magnets discussed in section 8.1.3.

8.3 Orbit Correction Algorithm

The following is a brief overview [28] of the orbit correction algorithms used both in the LHC Orbit Feedback System and in the MADX correction scripts used in this thesis.

8.3.1 Least Square Fit

A closed orbit responds linearly to a dipole corrector excitation. Therefore we can write an equation for orbit correction in the following way:

$$B\vec{P}M - \underline{A} \cdot C\vec{O}R = \underline{0} \, , \tag{40}$$

where $C\vec{O}R$ is a vector containing all corrector magnet strengths, $B\vec{P}M$ is a vector containing all BPM readings and $\underline{A}$ is the $n \times m$ response matrix for the closed orbit as a function of the excitation. The inverse of the response matrix should ideally be able to be used to calculate the necessary corrector settings for $C\vec{O}R$ that would minimise the closed orbit. However $\underline{A}$ is usually not invertible. As a consequence of this, we must take the square norm of the orbit correction equation and use a 'Least Square' fit that aims to minimise the following equation:

$$\|B\vec{P}M - \underline{A} \cdot C\vec{O}R\|_2 \, . \tag{41}$$

The pseudo-inversion of $\underline{A}$ is $\underline{B}$ and it can be used to minimise the quadratic norm and define the required corrector settings for a given closed orbit reading as:

$$C\vec{O}R = \underline{B} \cdot B\vec{P}M \, . \tag{42}$$

The 'Least Square' algorithm is useful as it is simple and powerful tools for matrix inversion are readily available. However, the algorithm uses all available corrector magnets and BPMs and is therefore susceptible to inaccuracy from wrong measurements in erroneous BPM data. Removing redundant BPMs in the 'Least Square' algorithm can cause linear dependency within the matrix which is not ideal. Therefore, in this case of instability, Singular Value Decomposition is used.

8.3.2 Singular Value Decomposition

Singular Value Decomposition (SVD) is essentially the 'Least Square' method but now the redundant corrector magnets are identified and removed from the algorithm. First the response matrix, $\underline{A}$, is decomposed into a product of two orthogonal, $\underline{O}$, and one diagonal, $\underline{D}$, matrix:

$$\underline{A} = \underline{O}_1 \cdot \underline{D} \cdot \underline{O}_2 \ . \tag{43}$$

The matrix $\underline{D}$ is defined so that it has k non-vanishing diagonal elements where k satisfies

$$k \leq \min(n, m) \ . \tag{44}$$

Another matrix $\widehat{\underline{D}}$ can be defined so that the following matrix expression is satisfied:

$$\underline{D} \cdot \widehat{\underline{D}} = \begin{pmatrix} 1 & 0 & \cdots & \cdots & 0 & 0 \\ 0 & 1 & 0 & \cdots & \cdots & 0 \\ 0 & 0 & 1 & 0 & \cdots & 0 \\ \vdots & \vdots & 0 & \ddots & \vdots & \vdots \\ 0 & \vdots & \vdots & \vdots & \ddots & \vdots \\ 0 & 0 & \cdots & \cdots & 0 & 1 \end{pmatrix} \ . \tag{45}$$

From here we can define the correction matrix $\underline{B}$,

$$\underline{B} = \underline{O}_2^t \cdot \widehat{\underline{D}} \cdot \underline{O}_1^t \ , \tag{46}$$

that minimises the quadratic norm and as before, defines the required corrector settings for a given closed orbit.

The SVD algorithm leads to a vector solution of the necessary corrector settings required to minimise a closed orbit without using anomalous BPM data.

8.3.3 Most Efficient Corrector Algorithm

However, harmonic filtering and Fourier analysis of the closed orbit response show that only a few orbit correctors are needed for a global correction of a random orbit distortion [29]. Therefore another method to minimise the norm (Eq. 41) is the most efficient corrector algorithm. This algorithm works by searching for the most effective corrector, adjusting the orbit, keeping this first corrector strength fixed and then searching for the next most effective corrector. This approach is used in the `MICADO` algorithm which can be implemented in MADX [30].

9 Datasets

9.1 Overview of Datasets

Tables 1 and 2 provide necessary information to find the datasets in the CERN eLogBook [31] and to extract the data in PyTimber. The information given below is taken directly from the eLogBook. All datasets are for LHC Beam 1 except for A*, which is for beam 2. E_B is the beam energy. 'Fill' is an abbreviation for fill number which is the name of LHC logbook folder for a particular machine development session [2]. t_1 is the initial time in the dataset and t_2 is the final time. δt is the time period for measurement. Q_x and Q_y are the measured horizontal and vertical tunes.

A short description of each of the optics used:

- Round ATS (Achromatic Telescopic Squeezing) optics allows the matching of β* while correcting chromatic aberrations [32].
- CT-PPS optics are the optics for the CMS-TOTEM Precision Proton Spectrometer [33].
- Ballistic Optics are used to understand optical errors and BPM systematic effects [34].

Dataset	t_1	t_2	δt (min:sec)	Date	Fill
A	13:08:23.289	13:35:49.115	27:26	15/06/2018	6800
A*	13:09:01.304	13:31:59:184	22:58	15/06/2018	6800
B	20:13:31:521	20:18:02:833	4:31	08/05/2017	5624
C	23:16:59:000	23:27:59:000	9:00	28/3/2016	4734

Table 1: This table provides time period information on the datasets used. It contains the necessary information to find the dataset in the CERN eLogBook [31].

Dataset	Q_x	Q_y	optics	energy status	E_B (TeV)	β* (m)
A	0.2805	0.3097	round ATS	flat-top	6.5	0.65
A*	0.2806	0.3093	round ATS	flat-top	6.5	0.25
B	0.2701	0.2948	CT-PPS2	flat-top	6.5	0.4
C	0.28	0.31	ballistics	flat-top	6.5	–

Table 2: This table provides the main machine parameters for each dataset.

The horizontal and vertical tunes for beam 1 for datasets A, B and C were plotted. A tune jump was only seen in dataset A. As the focus of this thesis is to look into sources that could cause large tune jitters and tune jumps, dataset A was chosen to investigate further. The tune data for dataset B can be seen in Figure 8 and the tune data for dataset C can be seen in Figure 9.

Figure 10 shows how the beta amplitude function for dataset A in both horizontal and vertical directions varies around the LHC. The amplitude functions are given in metres and were collected for this dataset using MADX.

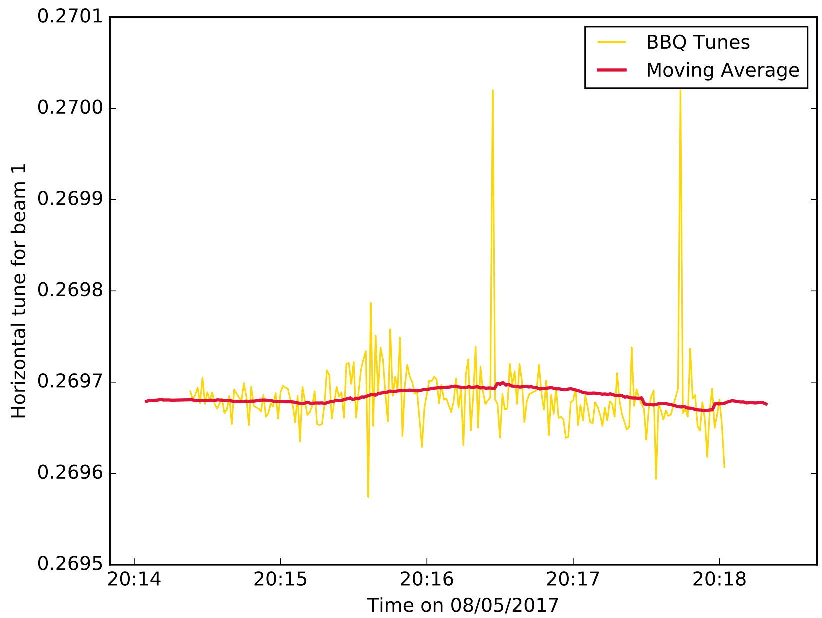

(a) Horizontal tunes for dataset B. Data was only recorded in PyTimber for 20:14:22 onwards.

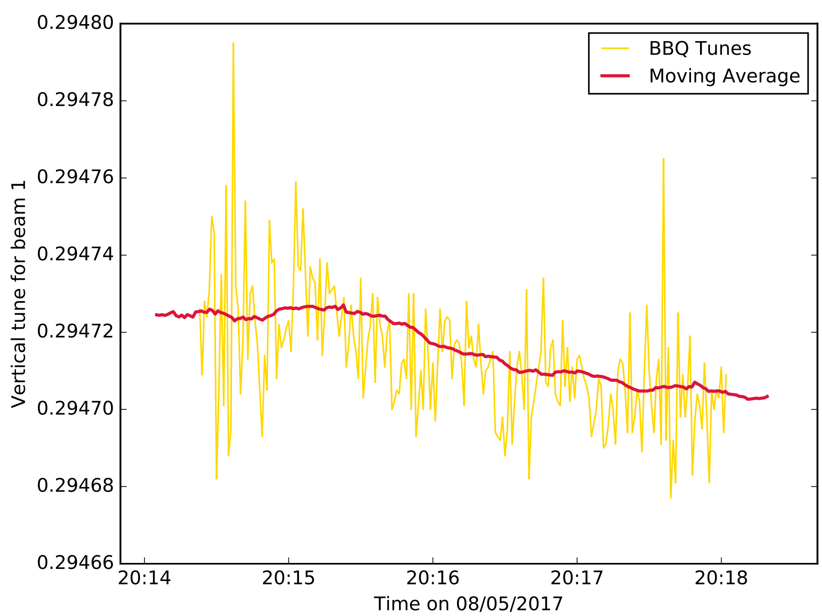

(b) Vertical tunes for dataset B

Figure 8: The horizontal and vertical tunes are shown here as the original data extracted from PyTimber with a moving average value over 50 points. The data is taken over the dataset B time period from 20:13:31 to 20:18:02 on the 8th of May 2017.

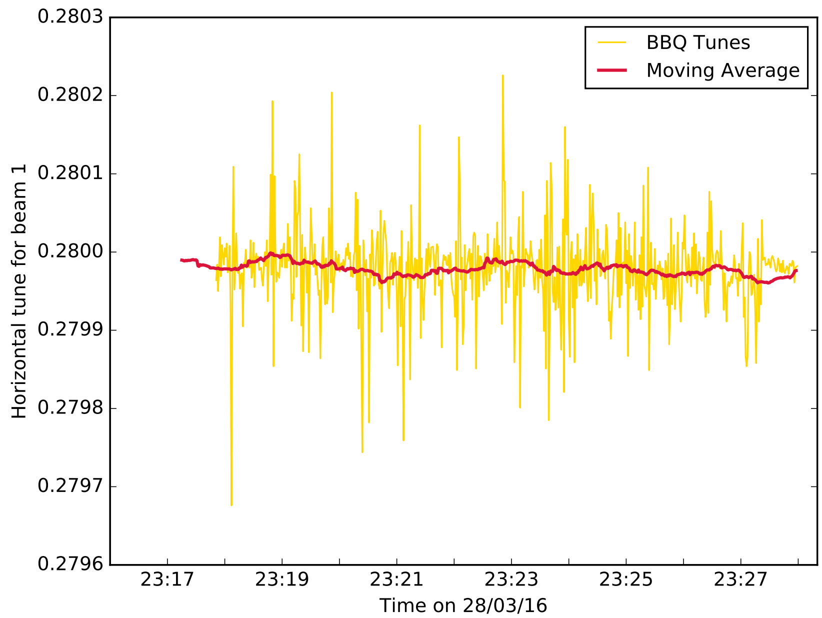

(a) Horizontal tunes for dataset C. Data was only recorded in PyTimber for 23:17:50 onwards.

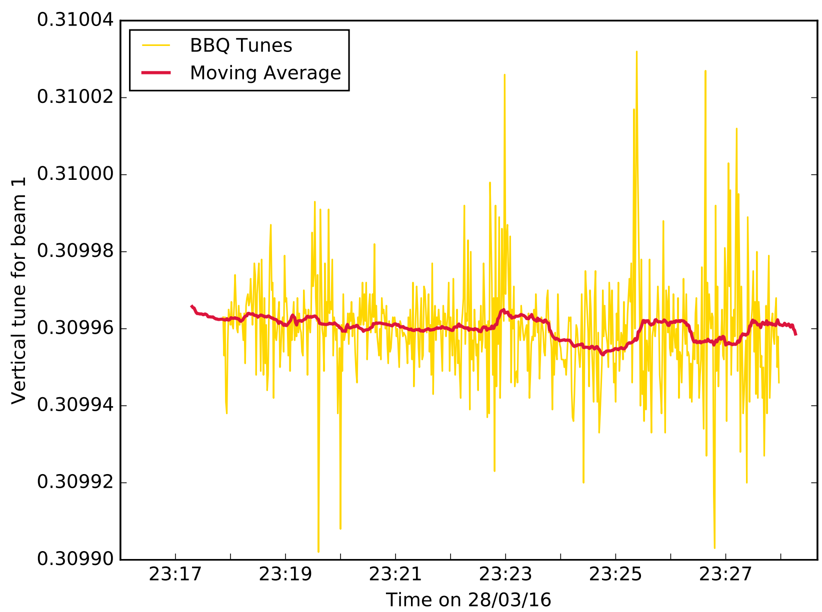

(b) Vertical tunes for dataset C

Figure 9: The horizontal and vertical tunes are shown here as the original data extracted from PyTimber with a moving average value over 50 points. The data is taken over the dataset C time period from 23:16:59 to 23:27:59 on the 28th of March 2016.

9.2 Dataset A beta amplitude functions

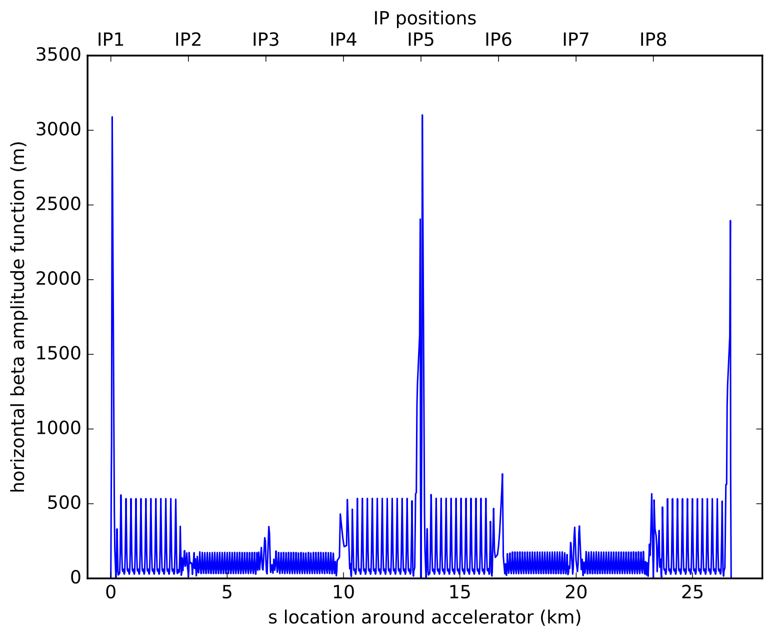

(a) Horizontal beta amplitude function β_x

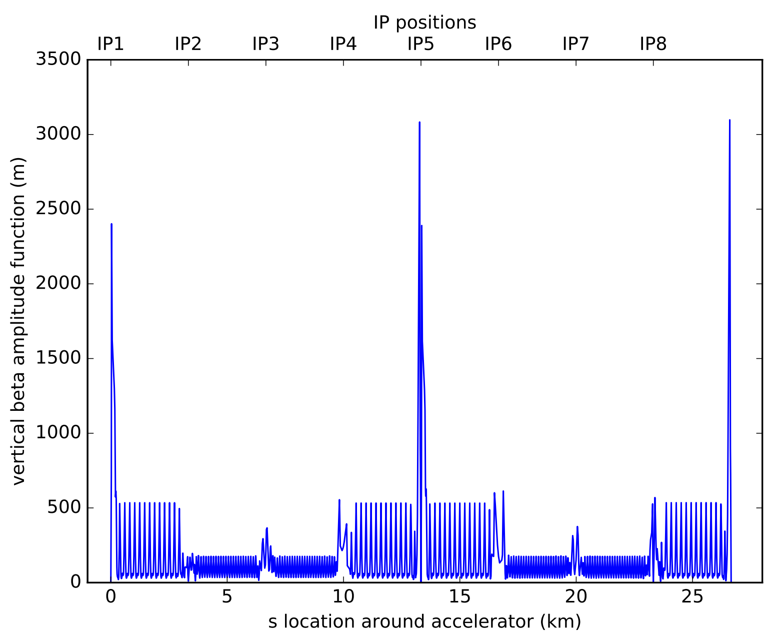

(b) Vertical beta amplitude function β_y

Figure 10: The beta amplitude function for dataset A in both the horizontal x and vertical y directions against the s location around the accelerator. The interaction points that occur along the LHC are also marked.

10 Methods, Results & Discussion

10.1 Initial Investigations into tune and orbit data

An initial graph looking into the horizontal tune over a specified time frame for dataset A was plotted. This dataset was chosen to build on existing work [2]. This dataset focused on optics data measured on the 15th of June 2018 for beam 1 of the LHC for 27 minutes and 26 seconds between 13:08:23 and 13:35:49 in the flat-top section of the cycle. All times were taken in the UTC time zone. See Table 1 and Section 9.2 for more information on dataset A.

The Base-Band Q (BBQ) measurement system [35] is a tune measurement system with the goal to measure the tune with a position sensitivity below 1 μm [36]. The tune data was extracted [2] from CERN's logging database, Timber, by using the python module, PyTimber [37, 38]. See Appendix A for names of Timber variables called to extract data throughout this thesis. The data was returned as an array with the first row containing information of the times at which the measurements were taken in seconds. The script included code that always printed the start and end time in seconds so that it could be confirmed that the data collected was for the correct timeframe. The second row contained data for the measured horizontal tunes for beam 1 at each time. These have no units as the tune is the number of betatron oscillation per turn.

Since the raw tune data contains peaks from AC dipole kicks and the jitters are large, an extra function [2] was included to calculate a moving average so that the progression of the tune with time could be understood more easily. This function cleaned any dipole kick anomalies by removing data larger or smaller than a value, `delta`, that is inputted as an argument upon calling the function. It can be shown that the kicks were indeed being removed by this part of the function by plotting the tunes without cleaning to show clear peaks.

Figure 11 shows the measured tune data before being cleaned to remove the 17 AC dipole kicks. The blue line shows the position of the tune jump that starts at 13:27:26. It is interesting to note that there is indeed an AC dipole kick at the exact time of this tune jump.

The moving average was calculated over 50 points using the python module, Pandas [39]. This function took a series of averages of different subsets over all tunes with each subset being 50 data points in size. In order to check that the function was in fact doing this, a few values given by the code were checked manually by simply adding up the measured tune values and dividing by 50. Since the averages matched for a few subsets taken at random, it was assumed that the code was working. The sensibility of the code was determined by comparing the produced and expected graphs. The function also removed any NaNs (Not a Number) that could have been in the data by using the built-in Pandas function `.dropna()`. This was done before and after the moving average to ensure that no NaN errors would be encountered.

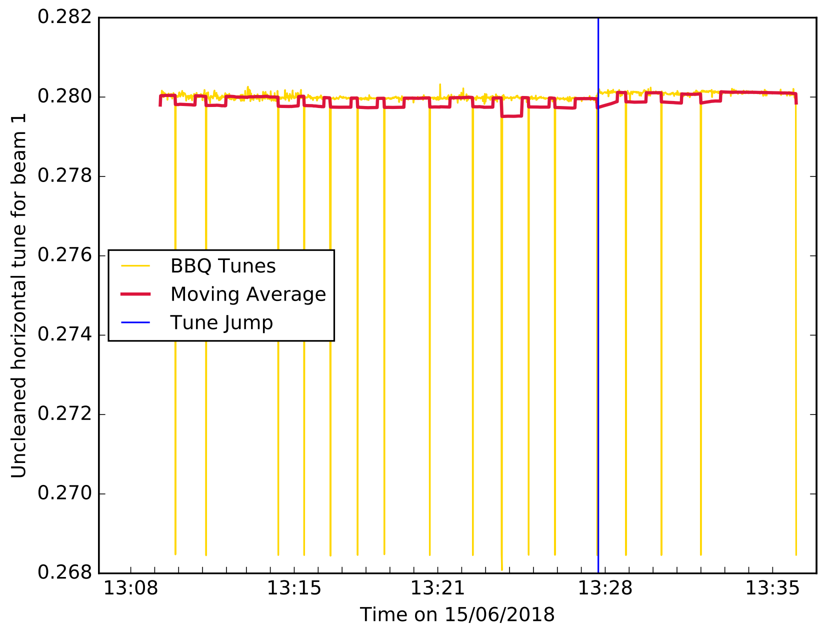

Figure 11: This graph shows what the raw horizontal BBQ tune data for beam 1 looked like before AC dipole peak cleaning happened. The tunes are shown with a calculated moving average against the dataset time frame. The blue line at 13:27:26 shows where the tune jump in Figure 12 occurred.

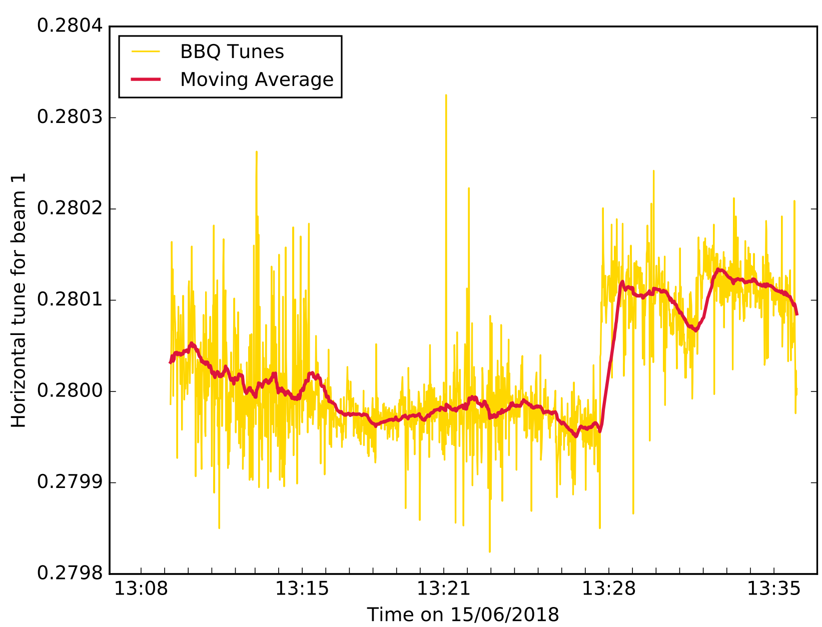

Figure 12: This graph shows the horizontal tune data for beam 1 extracted from Timber and measured by the BBQ system. The yellow plot shows the extracted data with AC dipole kicks cleaned. The red plot shows the moving average of these tunes. These both show the tune over the time period between 13:08:23 and 13:35:47 on the 15th of June 2018 where the first data point was for 13:09:14. Each tick on the x axis represents a minute.

Figure 12 shows the measured horizontal tunes and the moving average tunes over time. A clear jump in the tunes can be see at 13:27:26. This jump lasts for 6 seconds until 13:27:32. The presence of this distinct tune jump means the data here is sensible to investigate further for tune jitter sources. We can take the estimated uncertainty in the tunes to be the standard deviation of the tunes with the jump removed. This gives an uncertainty of $\pm$ 56 $\times$ 10^{-6}. The jump in the moving average, of 180 $\times$ 10^{-6} $\pm$ 56 $\times$ 10^{-6} oscillations per turn, goes from 0.27995 to 0.28013. For the measured tunes, this is a jump from 0.27985 to 0.28014 of 290 $\times$ 10^{-6} $\pm$ 56 $\times$ 10^{-6}. When determining where these tune jumps could have originated from, it is sensible to start with investigating the orbit as orbit errors are a possible source causing tune jitters and can be investigated well. Refer to section 7 for an overview of the possible sources of tune jitter.

The orbit data like the tune data was extracted with PyTimber using similar code for the same time period. Both horizontal and vertical orbit positions were extracted. The orbit positions measured by BPMs can be said to be at the given corresponding time since the typical collection time is less than 3ms [40].

The horizontal orbit position data was given as an array with the first row being the times in seconds from the specified start time. The second row was an array of BPMs for each time. Each BPM had a corresponding array of measured horizontal positions, given in micrometers. The number of BPMs in the array was 1088. This is because each BPM records beam specific orbit data - one set for beam 1 and one set for beam 2 [41]. This means there were 544 BPMs around the accelerator for each beam. In order to check that orbit data for all the BPMs was returned, BPM name data was also gathered. The BPM name data was also extracted using PyTimber and this returned a list of BPM names as strings. The number of BPMs in this data corresponded with the number of BPMs suggested in the orbit data.

The BPM names data here were only found in PyTimber for a time outside of the specified time frame for dataset A. The time frame was increased to the earlier time of 10:08 on the 14th of June. This did not have an effect on any other data as the extraction of the string data was completely separate to any other data analysis. This string data was then stored using the python module Pickle [42]. This ensured that in order to use the BPM name data in any further scripts for dataset A, the time frame would not need to be extended. Storing the data in such a way also meant that any further scripts would take a shorter time to run as the data would not need to be extracted from Timber each time.

In order to check that the actual orbit position data were sensible, the horizontal and vertical positions around the ring at all the BPMs for beam 1 were plotted for a random time chosen within the time period. The chosen time was 13:21:00. These preliminary investigations into the positions around the ring for the chosen time can be seen in Figure 13. All the graphs in Figure 13 contain cleaned data as the uncleaned orbit data showed anomalous peaks. Cleaning was done with a simple code that removed any results more or less than 2 standard deviations above the mean of the data. It was confirmed that the code did this accurately without changing the other data by printing the data points that the code had removed. It was also checked by observing that the graphs before and after the peak-cleaning were different and showed that any anomalies were removed. Cleaning to 2 standard deviations was chosen with reason as cleaning to 1 standard deviation removed too much data and showed no peaks and cleaning to 3 kept anomalous data. Figure 14 shows the orbits before cleaning occurred. The horizontal orbit for the time at which the tune jump in Figure 12 occurred (13:27:26) for beam 1 was also plotted to see if this orbit yielded any interesting observations that could be used to explain the tune jump. The cleaned and uncleaned orbit positions for the time at which the tune jump occurred can be seen in Figure 15.

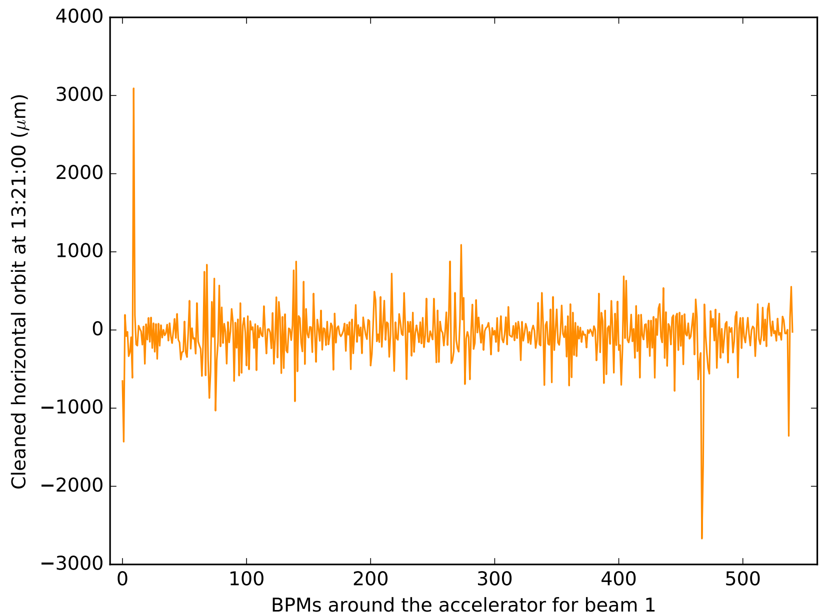

(a) Horizontal orbit for time 13:21:00

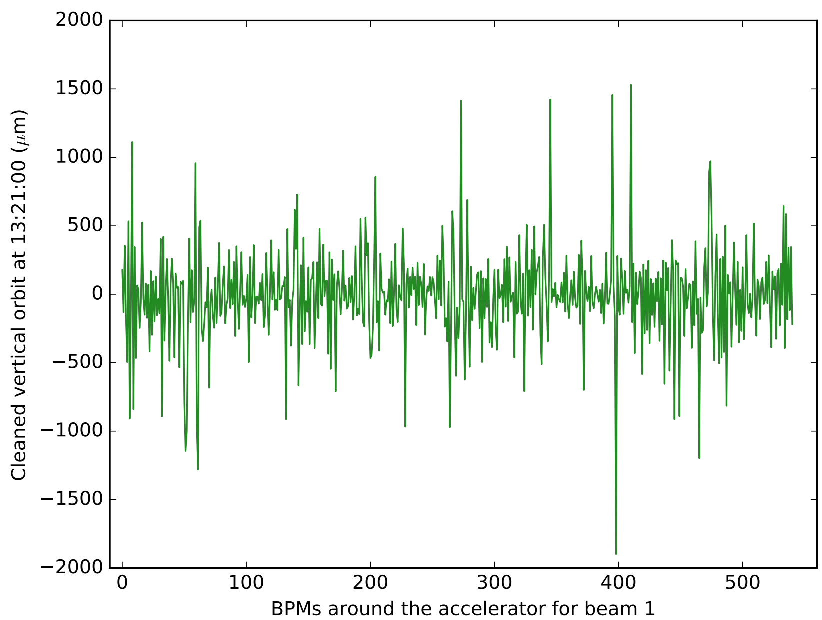

(b) Vertical orbit for time 13:21:00

Figure 13: These are the first graphs investigating the nature of the horizontal and vertical orbits at a time (13:21:00). All graphs are for beam 1 only. These are the orbits after data had been cleaned.

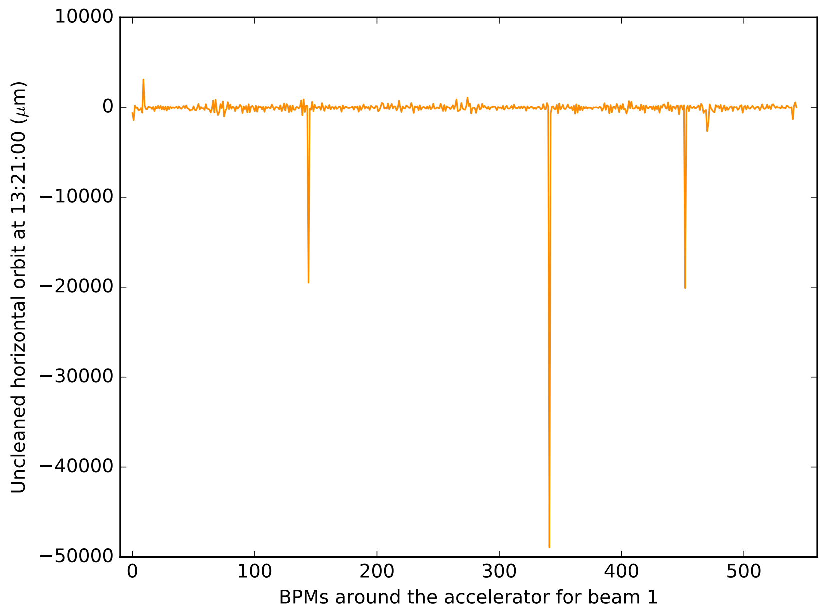

(a) Horizontal orbit for random time 13:21:00

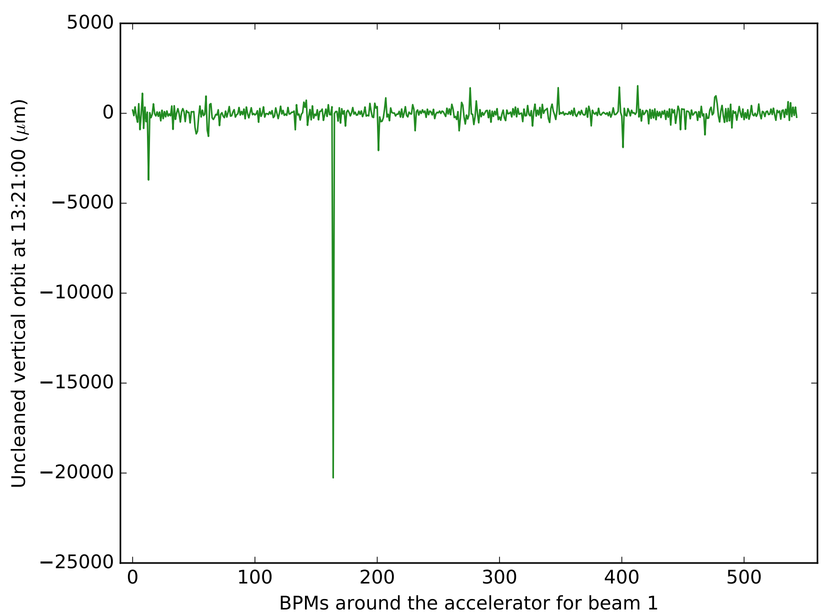

(b) Vertical orbit for random time 13:21:00

Figure 14: These graphs show the original orbit positions measured by BPMs and taken from Timber. The anomalous peaks that were cleaned in Figure 13 can be clearly seen here.

Figure 13 shows the horizontal and vertical orbits measured at BPMs around the accelerator after the data has been cleaned to 2 standard deviations. The cleaned horizontal data (13a) has a similar range of orbit jitters to the vertical (13b), with the majority of orbit positions for both horizontal and vertical directions lying between -1000 μm and 1000 μm. There are more peaks of a larger amplitude in the uncleaned horizontal orbit (14a) than the uncleaned vertical orbit (14b) with the largest horizontal peak at -49000 μm and the largest vertical peak at only -20500 μm. Figure 15, which shows the cleaned and uncleaned horizontal data for the time of the tune jump 13:27:27, is very similar but not identical to the horizontal orbit data for 13:21:00. These figures provide convincing evidence that the orbit data extracted from PyTimber is indeed sensible and can be used reliably.

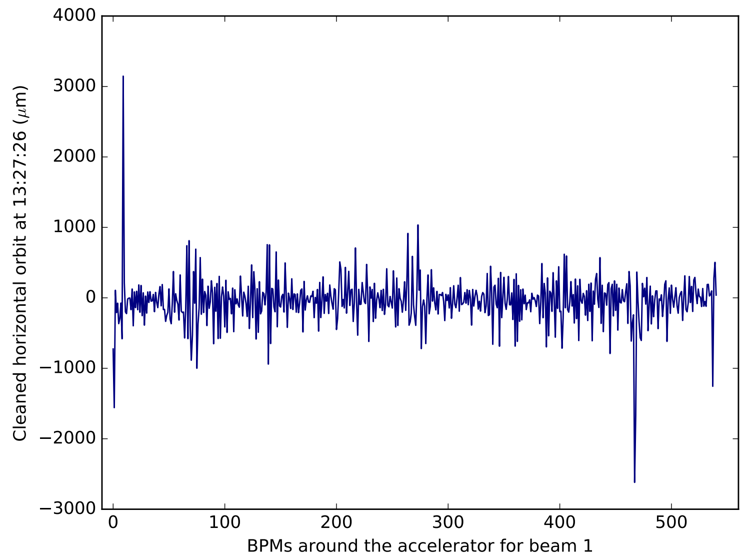

(a) Cleaned horizontal orbit

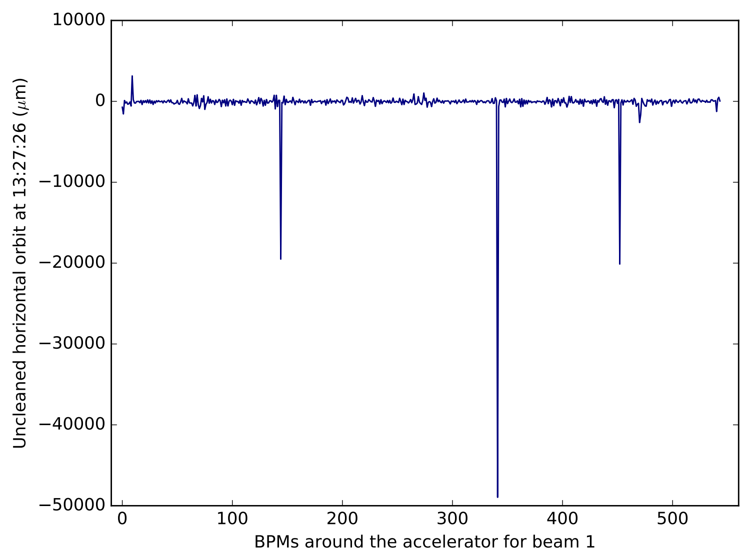

(b) Uncleaned horizontal orbit

Figure 15: The cleaned and uncleaned horizontal orbits for beam 1 are plotted here for the time at which the tune jump occurred (13:27:26).

10.2 Investigating links between orbit and tune data

So far only the horizontal tunes for beam 1 have been looked at. In order to get a clearer picture of the tune behaviour for dataset A, the horizontal and vertical tunes and their moving averages for both beams 1 and 2 were examined to see if similar tune jumps or large jitters were observable. Each of these graphs were plotted with corresponding orbit data to compare the correlation between orbit and tune. To explore whether there were any jumps or distortions in the orbit that could explain the tune jump, it was appropriate to see how the orbit positions changed with time. Therefore the ring average and the ring RMS were plotted against the appropriate tunes to determine if any orbit distortions were correlated significantly enough with the tune to merit from further investigation.

The ring average orbit was plotted by simply calculating the average position over all BPMs for each time using NumPy's built-in mean function, '`.mean()`' [43]. This function simply sums up all the orbit position values and divides that by the number of BPMs to give the average value. The same was done to plot the RMS but here the NumPy standard deviation function was used. Since there are several standard deviation functions in NumPy it is important to note that this function is '`.std()`', which calculates the square root of the average of the squared deviations from the mean [44], or:

$$\sigma = \sqrt{\langle (x - \langle x \rangle)^2 \rangle}\ , \tag{47}$$

where x is the dataset in question and $\langle\ \rangle$ is the average.

All the graphs showed at least a slight jump in the tunes for the time period 13:27:26 to 13:27:32. These were not prominent and of small amplitude in Figures 16b and 17b for the beam 1 vertical tunes. The orbit jitters here did not correlate so the beam 1 vertical direction was not chosen to look into further. The tunes measured for beam 2 showed clear jumps in both the horizontal and vertical directions for the same jump time period. The vertical tune jump was distinct but the orbit in Figures 18b and 19b only showed a clear correlating orbit jump in the RMS. The jump seen in the horizontal tunes for beam 2 was in fact larger than the jump in the beam 1 horizontal tunes. There was not a correlation in the ring average orbit but there was some correlation in the RMS. As there seem to be correlating jumps in the tunes and RMS orbit, both the horizontal and vertical tunes for beam 2 could be looked at further. The large orbit jumps that can be seen in Figures 18a and 19a are very large and most likely operational. Since there is no correlation with the tunes for these orbit displacements, we will ignore this.

Figure 16a which shows the beam 1 horizontal direction was chosen to continue probing as both the orbit jump in the ring average and the tune jump were very clear and correlated well. The Pearson correlation coefficient (r-value) was calculated to show how well both the moving average tunes and the measured tunes correlate with the ring average horizontal orbit. The Pearson correlation coefficient is a simple way to determine the linear relationship between two datasets. Like other correlation coefficients, this one varies between -1 and +1 with 0 implying no correlation. Correlations of -1 and +1 imply an exact inverse or direct linear relationship, respectively. The p-value was also calculated. The p-value roughly indicates the probability of an uncorrelated system producing datasets that have a Pearson correlation at least as extreme as the one computed from the datasets in question. The p-value is considered reasonably reliable for datasets greater than around 500 values, which is true in this case [45]. The values calculated can be found in Table 3. The r-values and p-values found suggest that the tunes and orbit correlate very well and so it is likely that the orbit jitters either have an effect on the tunes or the same other source is affecting both variables similarly.

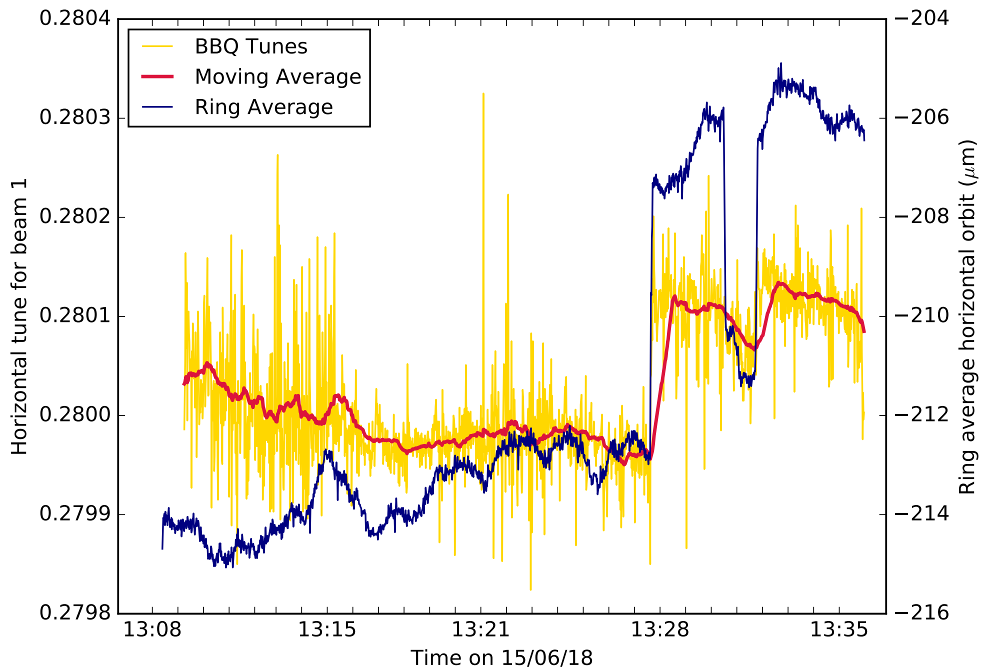

(a) Beam 1 horizontal tunes and ring average horizontal orbit

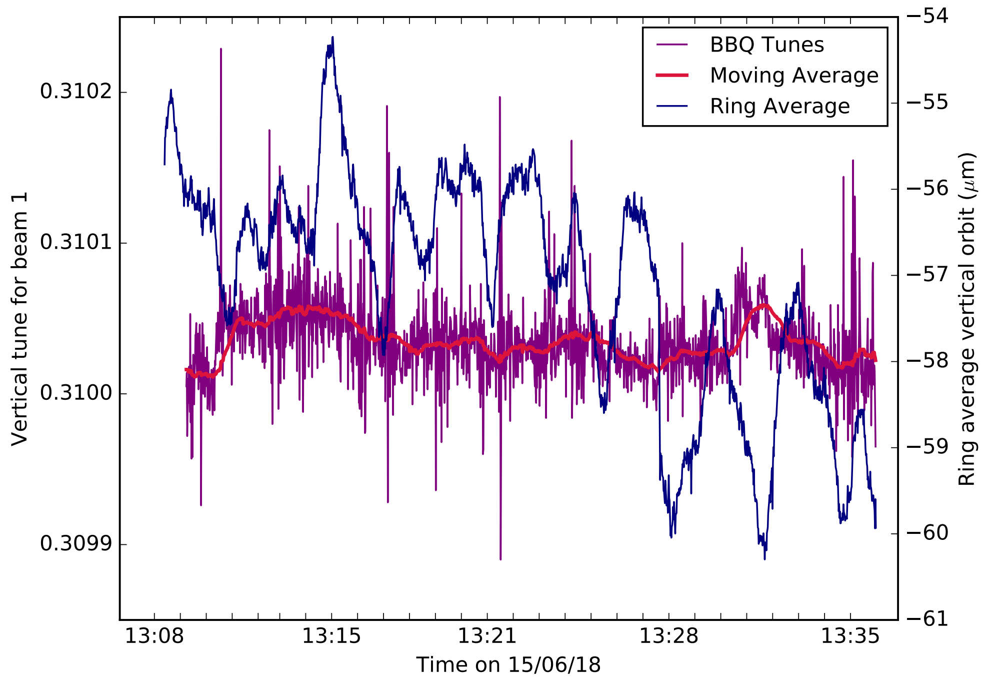

(b) Beam 1 vertical tunes and ring average vertical orbit

Figure 16: The ring average of the orbit in a given direction is plotted with the BBQ measured tune and its moving average in that direction for beam 1 The orbit positions are given in micrometers. Both plots are shown against the time on the 15th of June 2018.

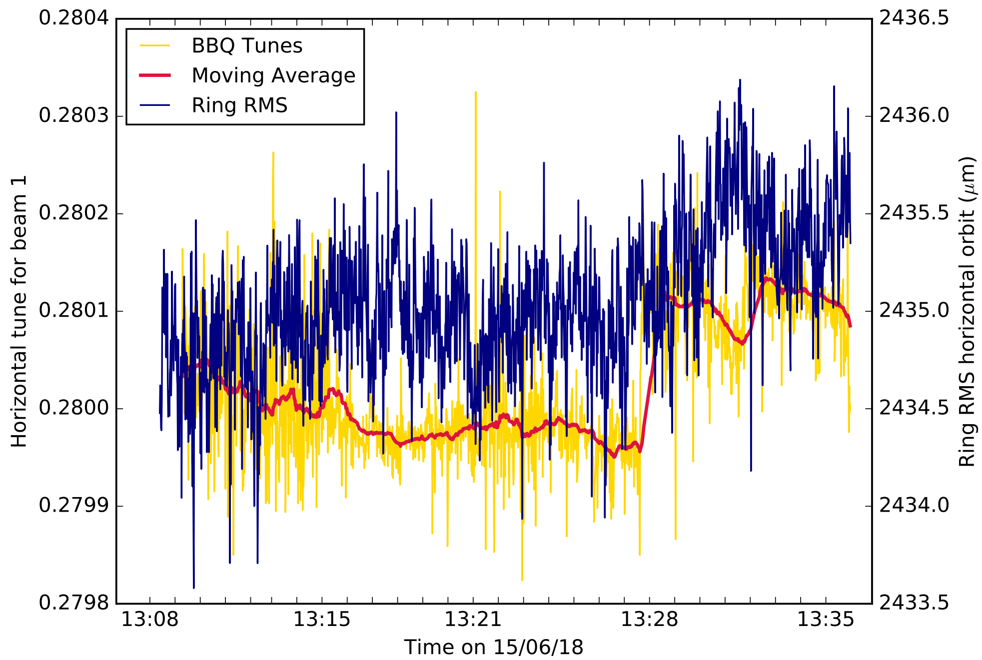

(a) Beam 1 horizontal tunes and ring RMS horizontal orbit

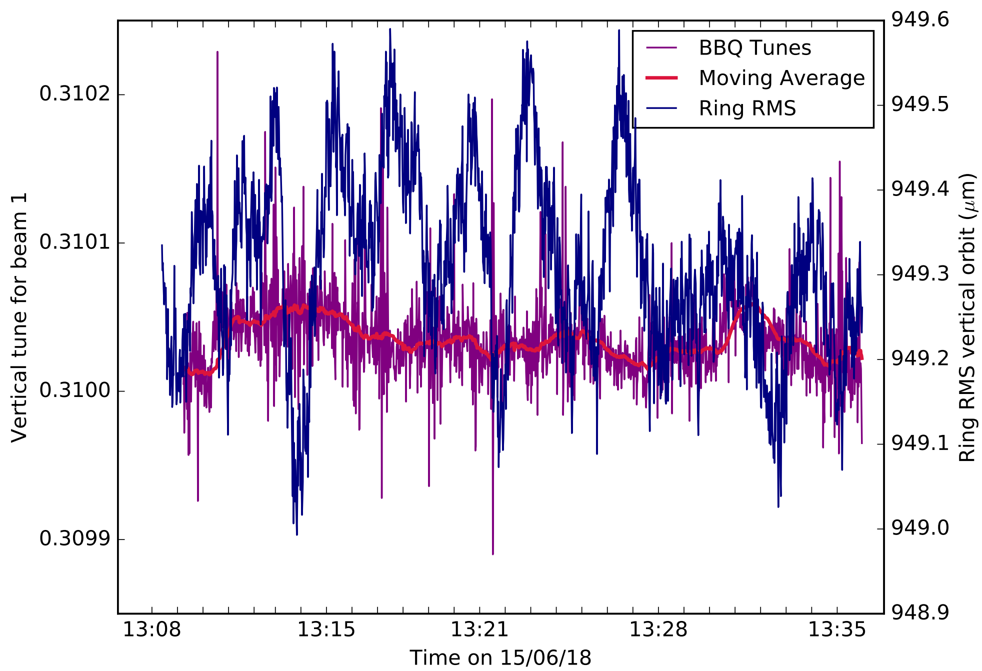

(b) Beam 1 vertical tunes and ring RMS vertical orbit

Figure 17: The ring RMS of the orbit in a given direction is plotted with the BBQ measured tune and its moving average in that direction for beam 1. The orbit positions are given in micrometers. Both plots are shown against the time on the 15th of June 2018.

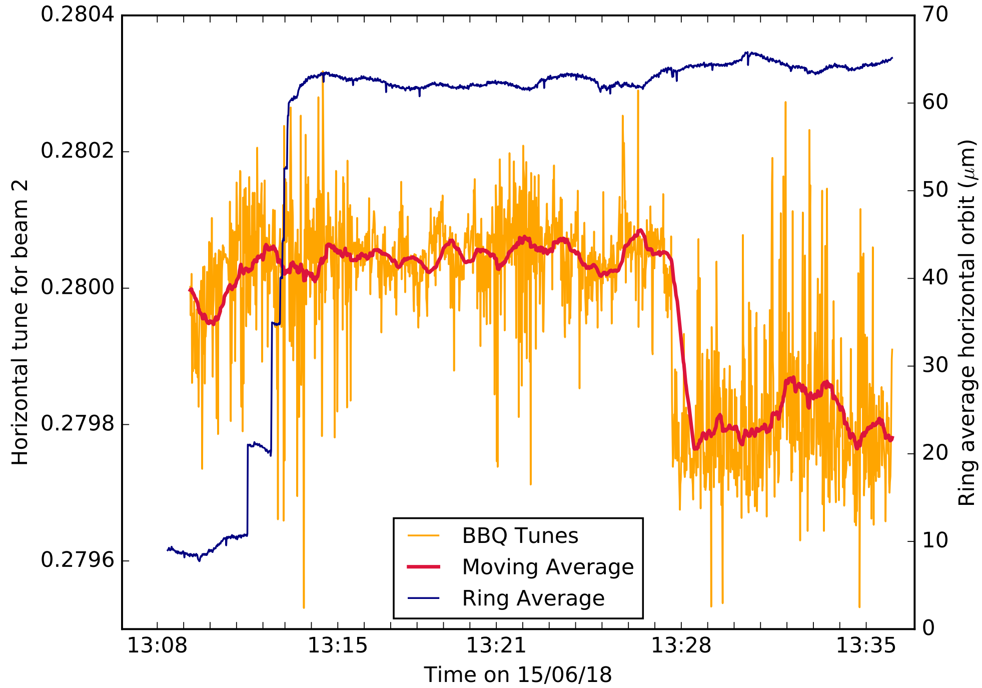

(a) Beam 2 horizontal tunes and ring average horizontal orbit

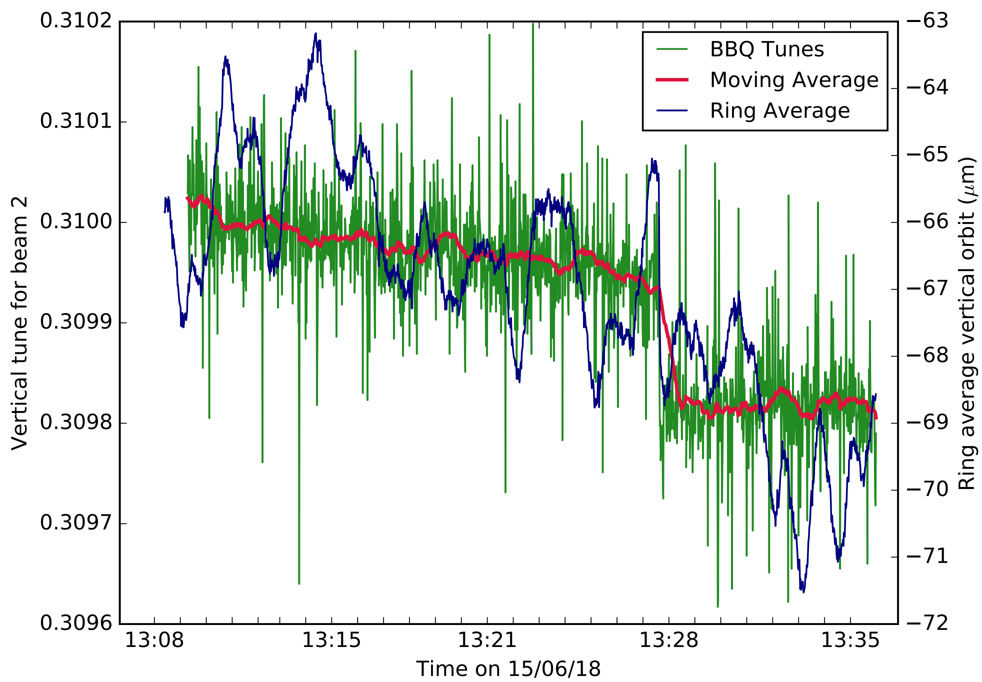

(b) Beam 2 vertical tunes and ring average vertical orbit

Figure 18: The ring average of the orbit in a given direction is plotted with the BBQ measured tune and its moving average in that direction for beam 2. The orbit positions are given in micrometers. Both plots are shown against the time on the 15th of June 2018.

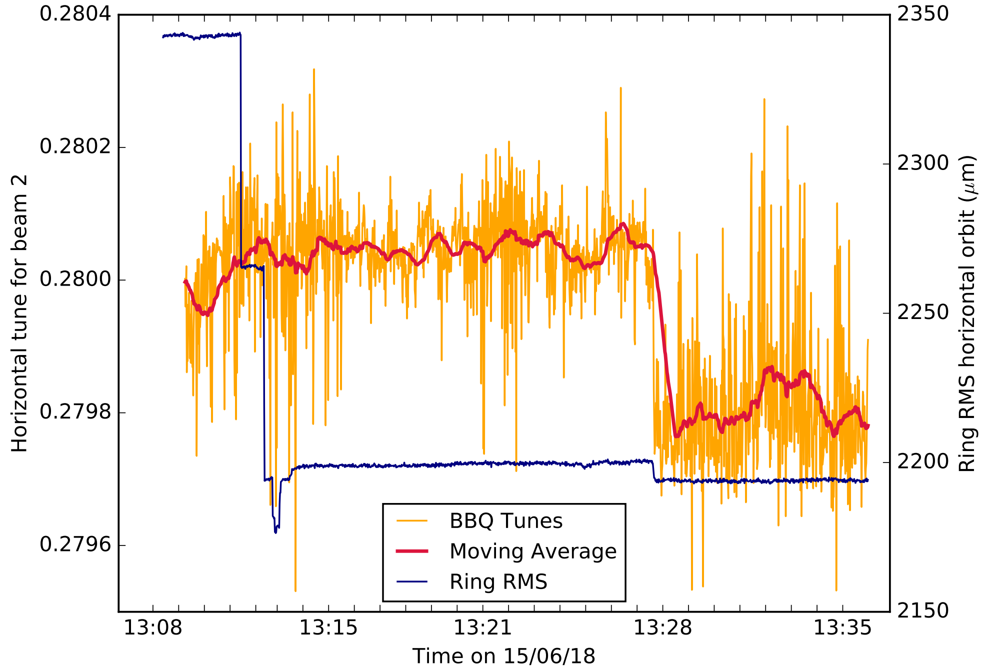

(a) Beam 2 horizontal tunes and ring RMS horizontal orbit

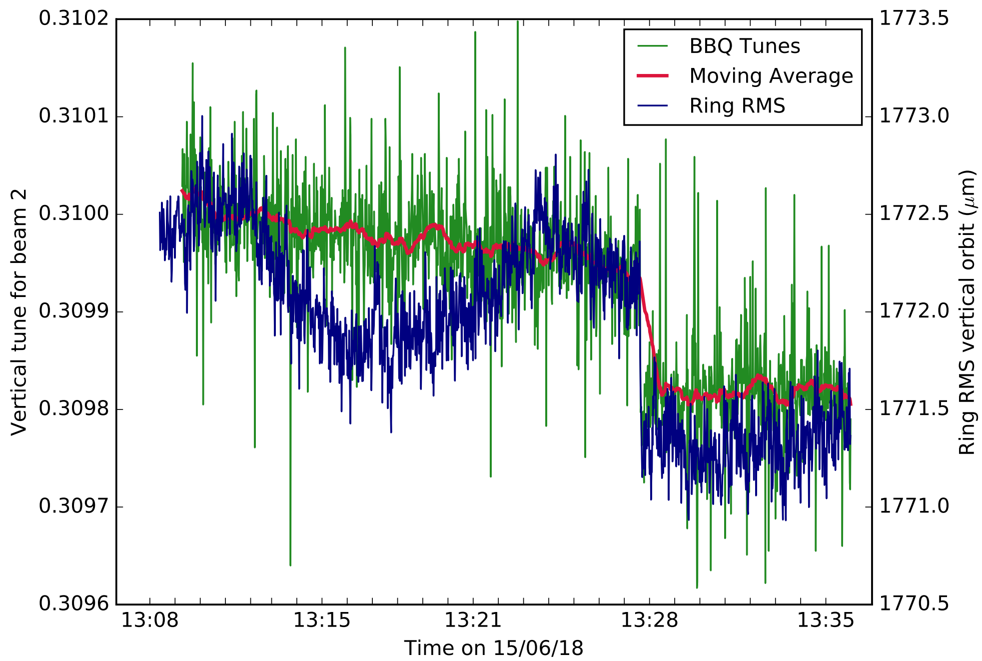

(b) Beam 2 vertical tunes and ring RMS vertical orbit

Figure 19: The ring RMS of the orbit in a given direction is plotted with the BBQ measured tune and its moving average in that direction for beam 2. The orbit positions are given in micrometers. Both plots are shown against the time on the 15th of June 2018.

	r-value	p-value
MAV	0.886	1.15×10^{-311}
BBQ	0.810	9.58×10^{-217}

Table 3: This table shows the r- and p-values calculated between the moving average of the horizontal tunes (MAV) and the ring average horizontal orbit and between the measured horizontal tunes (BBQ) and the ring average horizontal orbit. The correlations here correspond to datasets plotted in Figure 16a.

The jumps that were seen in the horizontal orbits could be more clearly analysed by plotting the ring average orbit difference. This was calculated by taking the difference between the average of the horizontal positions measured over all BPMs at a time, $x(t)$ and the position at the initial time, $x(t_0)$ i.e:

$$\langle x(t) - x(t_0) \rangle \ . \tag{48}$$

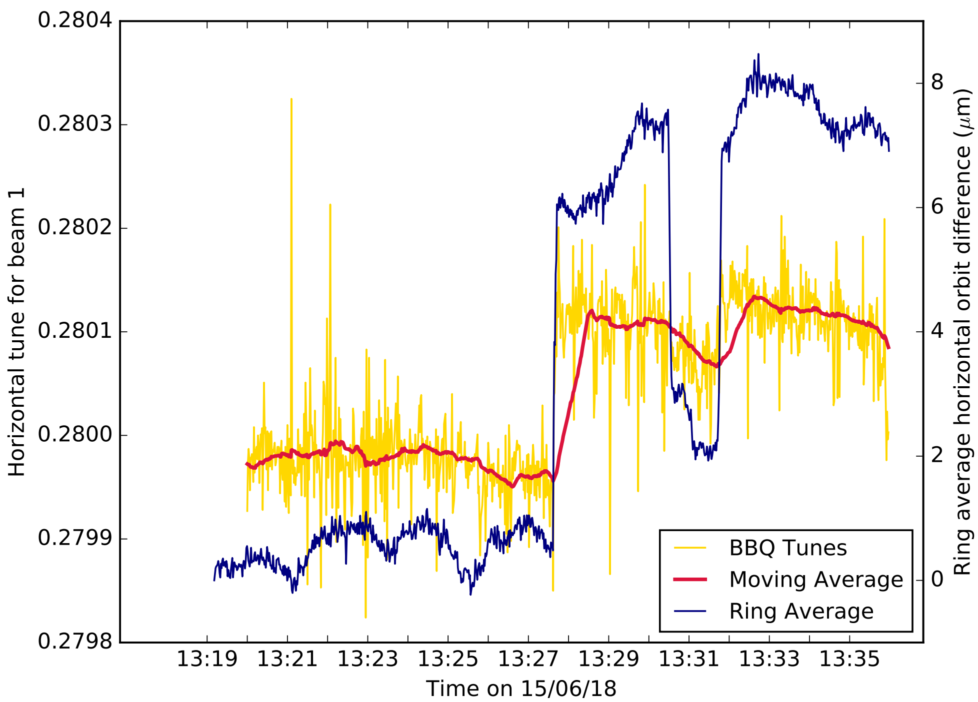

Figure 20: This graph compares the beam 1 average horizontal orbit with the horizontal measured tune and moving average for a smaller time period of 13:19:00 to 13:35:49. This is to focus on the time around the jump.

Since the main area of interest is the time period where the jump in the orbit coincided with the jump in the tune, a new time period encompassing this jump area was focused on. This was the period between 13:19:00 and 13:35:49. Figure 20 shows a jump in both the orbit (5.57 μm) and the tunes (0.00018) from 13:27:26 to 13:27:32. This jump in the orbit has an uncertainty that is difficult to compute exactly due to machine fluctuations. However, we can approximate an optimistic uncertainty to the BPM resolution. The BPM resolution is ideally 1 μm for each BPM. The average resolution over BPMs would be reduced by $\sqrt{N}$, N is the number of BPMs: 544. This means the uncertainty on the ring average orbit jump would be $(1/\sqrt{544})$ μm which is roughly 0.04 μm. Therefore we can say that the orbit jump is 5.57 μm $\pm$ 0.04 μm.

There is a large orbit jump down and then up of a similar amount to the jump that occurs at 13:27:26. However, there is no similar strong correlation in the tunes. This could be looked into further to understand why this happens.

10.3 Calculating tune shift, δQ

It is possible that the tune jump is due to the feed-down effect. Orbit distortion in sextupoles generates a quadrupolar component in the sextupole magnetic field. This can be shown by examining the field strength of a sextupole that experiences an orbit displacement as done in section 7.2. Therefore the tune shift of the machine at the time at which this orbit jump occurs (13:27:26) was calculated to see if it matched the tune shift in the measured tunes and to determine whether the feed-down effect was a possible reason for the tune jump.

First it was necessary to obtain a graph that showed how the orbit jump varied around the accelerator. This was done by plotting the difference between the at the beginning and the end of the jump times against the location around the accelerator. Each location around the accelerator refers to the location of BPMs.

The orbit differences, which may henceforth be referred to as jumps, were saved as a pickle file to avoid the long time that it takes to extract the data from PyTimber each time the script is run.

Both the saved files of BPM string names and jumps at each BPM were used to plot the graph of jump against 's' location. A MADX script was used set up the situation so the correct sequence for the beam 1 LHC was used. To ensure that the BPM that measured the first datapoint in the jumps data was the same as the first BPM whose location would be returned in MADX, the 'CYCLE' command [46] was used to align the BPMs. It was confirmed that the BPMs that read the orbit positions and the BPMs in MADX were aligned by printing the names of BPMs and checking that they lined up.

The MADX script generated a Twiss file that outputted selected variable data for each BPM. This data included each BPM name with its corresponding 's' location. By using the Twiss class from the Python module metaclass [47], a list of 's' locations for each BPM could be gathered the Twiss file. Therefore each horizontal position difference was plotted against the 's' location around the accelerator of the BPM that measured it. This can be seen in Figure 21. This was done not only to have corresponding jumps and s location data but also to analyse the behaviour of the orbit jump around the accelerator.

The orbit jumps seem fairly consistent from IP1 to IP4 and from IP6 to IP8 with jumps at roughly $\pm$ 5-6 μm. The average jump decreases to around $\pm$ 3 μm between IP4 and IP6. The largest jump seems to occur at IP5 and is around $\pm$ 10 μm. A similar sized jump occurs at IP1. It makes sense that the behaviour of the orbit jump at IP1 and IP5 are similar. This is because the Interaction Regions (IRs) 1 and 5 are both identical in terms of hardware and optics, since they are both locations of high luminosity experiments [48] - ATLAS and CMS, respectively. It can also be seen in Figure 10 that the β function spikes at the interaction points.

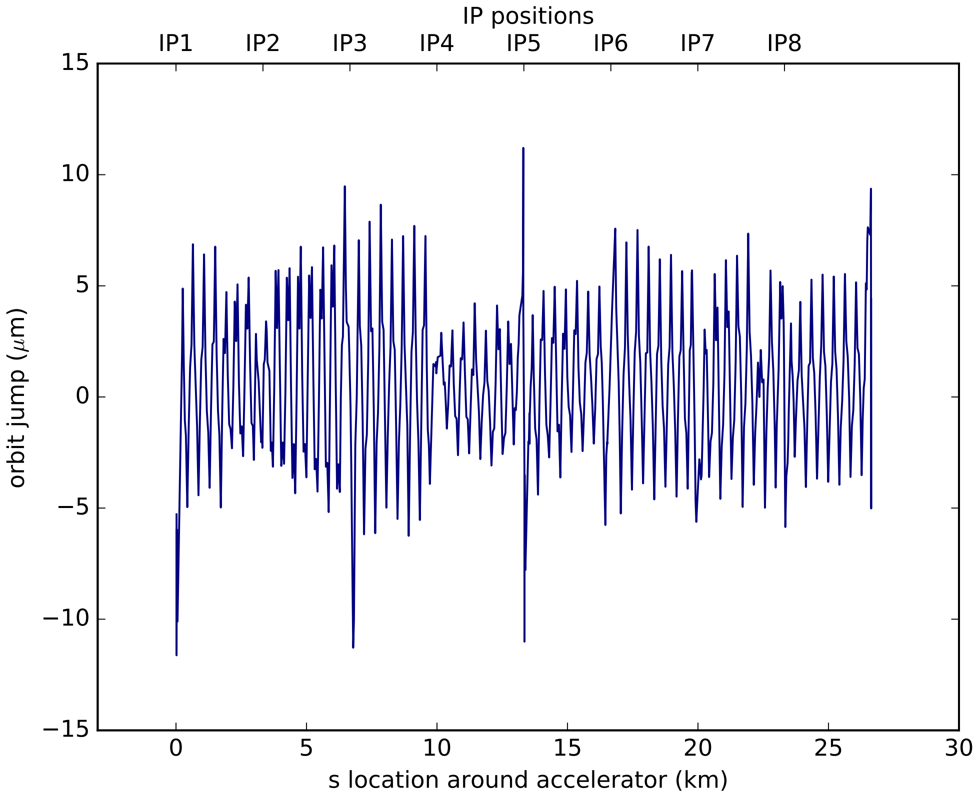

Figure 21: This graph shows the difference in horizontal orbit position between the times 13:27:26 and 13:27:32. It shows how the jumps varied at different points around the 's' location of the accelerator. Interaction point 1 was chosen to be the starting point, i.e: $s = 0$ km, and also the ending point, $s = 26.7$ km, where 26.7 km is the circumference of the LHC. The location of the 8 interaction points (IPs) are clearly marked on the graph and these 8 sections are also reflected in the shape of the orbit jitters.

Since we are interested in the extent to which the orbit misalignment affects the tunes, we can calculate the horizontal tune shift that we expect from this jump. This is done by calculating the tune shift from each sextupole and then summing it to get the global tune shift. The equation for the horizontal tune shift due to feed-down is given by summing Eq. 33 over selected sextupoles (i):

$$\Delta Q_x = \frac{1}{4\pi} \sum_i (k_2 L)_i \cdot (\beta_x)_i \cdot (dx)_i \ , \tag{49}$$

where $k_2 L$ is the sextupole strength, β_x is the unperturbed beta constant at the sextupole location and dx is the orbit misalignment of the sextupole.

The strengths and beta constants could be extracted from a Twiss file. The orbit misalignments are just the orbit jumps that have already been linked to a BPM 's' location. The selected sextupoles must be close to a BPM. This is simply because we need the misalignment at a sextupole and this is just the misalignment at a BPM near to a sextupole. For a sextupole to be classified as close to a BPM, it needed to be closer than 5 m. All other sextupoles, 8 in total, were excluded. This was done by generating a Twiss file using MADX that selected all the sextupoles around the accelerator. This

Twiss file contained the name, s location, horizontal beta constant and sextupole strength of all the sextupoles around the LHC.

The data needed to compute the tune shift was extracted from this Twiss file into NumPy arrays that behaved as vectors with a horizontal 'x' and a vertical 'y' component in order to calculate both the horizontal and vertical tune shift. The sextupole strength was the same in both horizontal and vertical directions for each sextupole. The orbit misalignment was just the horizontal orbit jump for both directions. The unperturbed beta constant had different values in the x and y planes and it is this variable that would make the horizontal and vertical tune shifts different. Since we are interested in comparing what we compute with the horizontal tune shift observed, we only calculate ΔQ_x.

With this data, the horizontal tune shift was calculated at each sextupole and then summed over all included sextupoles to give a total tune shift of the machine. The result was a total horizontal tune shift of 654×10^{-6} oscillations per turn.

10.4 Calculating tune shift, δQ, over time

In order to see how the the orbit data over the whole specified time period should affect the tune, the total horizontal tune shift was plotted with time. This was done by using a similar method to the one previously and by modifying Eq. 49 in the following way:

$$\Delta Q_x = \frac{1}{4\pi} \sum_i (k_2 L)_i \cdot (\beta_x)_i \cdot (dx(t))_i \ . \tag{50}$$

The calculation again required three vectors of data for sextupole strengths, unperturbed beta constants and orbit misalignments. The orbit misalignments were calculated in a similar way to the jumps described above. However, instead of calculating the horizontal orbit position difference, dx between one set time period, a set of differences or 'jumps' were calculated as a function of the time. Therefore $dx(t)$ was defined as $x(t) - x(t_0)$ for each time, t, where t went from the initial time of the time period, t_0 and the maximum time of the time period. The sextupole strengths and the unperturbed beta constants were again extracted from a MADX script and only the sextupoles less than 5m away from a BPM were used.

Figure 22 shows that the beam 1 ring average orbit and the tune shift correlate well with a high Pearson r-value of 0.954. The orbit jump and the steep increase in tune jump occur at the same time of 13:27:26. The expected tune shift from the orbit jump was calculated to be 677×10^{-6}, which is close to the expected tune shift at the jump that was calculated in the previous section. The tune shift here is however much smaller than the tune shift that was observed in the measured tunes in Figure 12, which means there could potentially be some inaccuracy in using this formula method to compute the expected tune shift from the orbit. This is possible since Eq. 50 to calculate the tune shift due to the feed-down effect is approximate. Another method to calculate the expected tune shift form this orbit data was followed to check the accuracy.

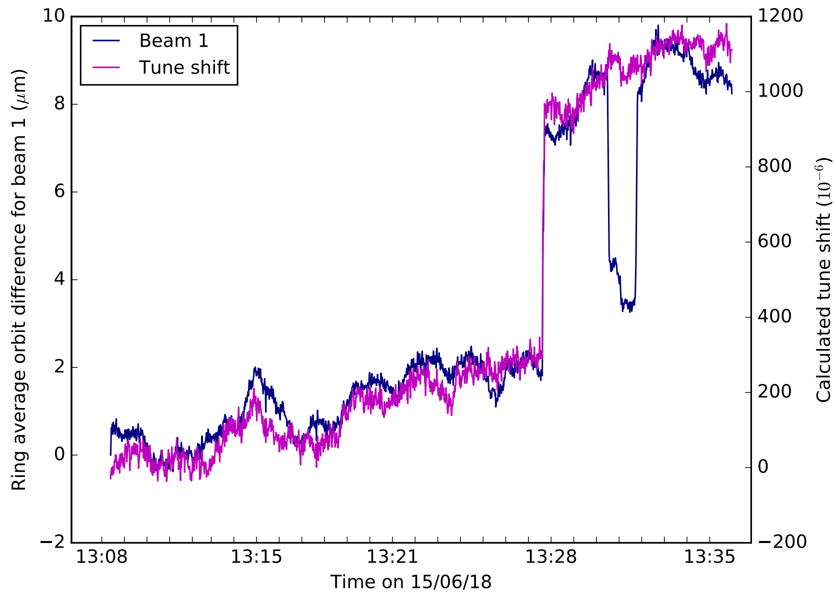

Figure 22: This graph shows the variation of the average of the difference between the beam 1 horizontal orbit at a time, t and an initial time, t_0 with the tune shift calculated from Eq. 50.

10.5 Investigating tune shift, δQ, further with a MADX Orbit Correction Module

The total horizontal tune shift expected from the observed orbit data was plotted with time, using MADX orbit matching [49]. This was done to confirm that the expected tune shift graph plotted by calculating the values from Eq. 50 was accurate. This method would also give improved results as the orbit is corrected first.

To correct an orbit and calculate the tune shift from this orbit, a MADX script was used which needed a CSV file of the observed dataset A orbit data from Timber. This CSV file contained orbit data for every BPM at each time. MADX would then select the orbit positions for a given time and correct them.

A python script was used to first ensure that any inputted times were formatted correctly into written strings as MADX would only read time passed through in a particular format to match the inputted time to the time corresponding to the orbit data in the CSV file. The times were taken from Timber to ensure that the times passed through to MADX were accurate to the millisecond.

The MADX script worked by taking in orbit data from every BPM from a CSV file for a specified time and correcting it. The correction process involves MADX calling a python script that filters erroneous BPMs and another script that uses virtual correctors to correct the orbit. The orbit is reconstructed by the orbit correction routine in MAD-X [**orbtmat**, 30]. The corrected data is then saved into a Twiss file that is generated by the script.

A python script replicated the MADX script and ran it for every time. The corrected tune was extracted from the generated Twiss file and the tune shift could be calculated by plotting the difference between the tune at a time and an initial time. The time, t, was taken up to 13:29:58 and the initial time, t_0 was taken as 13:21:00. This shorter period was used because the correction script had to be run for each second and took roughly 3 minutes to run for each data point. To reduce times further, orbit data for every other second was used but for the time between 13:27:26 to 13:27:32, each second was plotted.

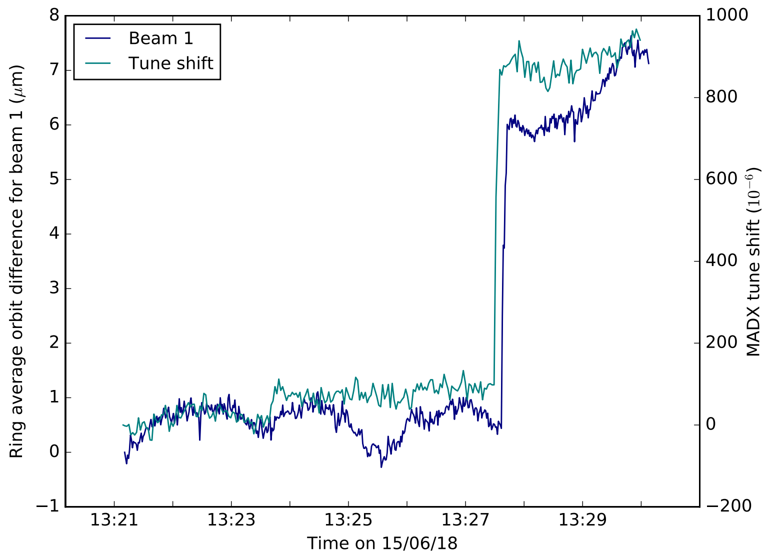

Figure 23: This graph shows the variation of the average of the difference between the beam 1 horizontal orbit at a time, t and an initial time, t_0 with the tune shift computed using tunes returned by MADX after it has corrected the observed orbit data.

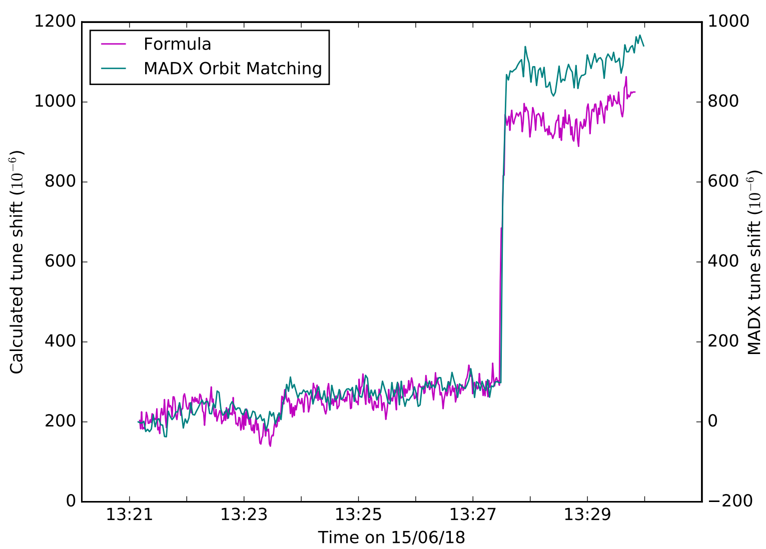

Figure 24: This graph compares the expected tune shifts from the observed orbit data using two different methods. The tune shifts with time calculated using the approximate formula for tune shift from the feed-down is shown in magenta. The tune shifts with time computed using MADX orbit matching is shown in teal.

Figure 23 shows the beam 1 ring average horizontal orbit and the tune shift predicted from the horizontal orbit data using MADX orbit matching. It can be seen that they correlate well as expected. It is more important to compare Figures reffig: beam1ts and 22 to check that they agree well. This comparison is shown in Figure 24.

Figure 24 shows that the two expected tune shift graphs have a high correlation. There are similar values of the tune shift for each orbit position change in the time period used. There is some difference in the expected tune shift at the time of the orbit jump. The tune shift returned by MADX from the orbit jump was 771×10^{-6} compared to that of 677×10^{-6} from the tune shift predicted from formula. These results are discussed further in the following section.

10.6 Effect of the Orbit on the Tune

So far, we have looked at the measured tunes and the orbit behaviour for dataset A and decided to focus on the horizontal direction for beam 1 as there is both a clear tune jump and a clear orbit jump for a 6 second period from 13:27:26 to 13:27:32. Beam 2 also showed a clear tune and orbit jump and its data should be studied further. In order to investigate the strong correlation between orbit and tune, we looked at the tune shift that the orbit jump alone would theoretically induce. The tune shifts computed using Eq. 50 and the tune shifts using MADX orbit matching both show how we expect the tunes to be affected by the observed orbit data. In order to test the hypothesis that the tune jump was caused by the orbit jump, we can compare the predicted tune shift with the actual measured tune jump from Figure 12.

From Figure 12 the tune jumps from 0.27985 to 0.28014 in the measured tunes and 0.27995 to 0.28013 in the moving average. If we take the moving average values, this meant the measured tune shift was 0.00018 or 180×10^{-6} at the time of jump.

The calculated tune shift (Figure 22) shows a tune jump of 677×10^{-6} and the MADX calculated tune shift shows a jump of around 771×10^{-6}. The MADX corrected tune shift is around 100×10^{-6} greater than the calculated tune shift.

The tune jumps expected from just the orbit data were much greater than the tune jumps measured and can be considered to be of accurate magnitudes since they were measured using different methods. One conclusion from this is that the lattice sextupoles together with orbit jumps are not the only source contributing to the tune jitters.

Following these results, sources that could have directly affected the tune were probed. Sources that eventually returned negative results have been included for thoroughness and as possible tests to be used for future datasets.

10.7 Tune Quadrupoles

Tune quadrupoles have a direct effect on the tune. As described in section 8.1.3, these are used to adjust the tunes of both beams so have the potential to be the reason the tune jump is smaller than predicted from the orbit jitters. The current change over the 15 minute time period of 13:20 to 13:35 in 8 RQTF and 8 RQTD tune quadrupoles were examined. The maximum current change over this time period was calculated by simply taking the range. A list of the magnets used here are included in Appendix B.

It was found that there were no changes in the currents through the magnets over this time period as the current values remained constant. The currents through both the RQTF and RQTD optical correctors were nonetheless plotted for thoroughness and can be seen in Figure 25. This suggested that these optical correctors were not responsible for adjusting the tune and being an additional source contributing to the tune jump.

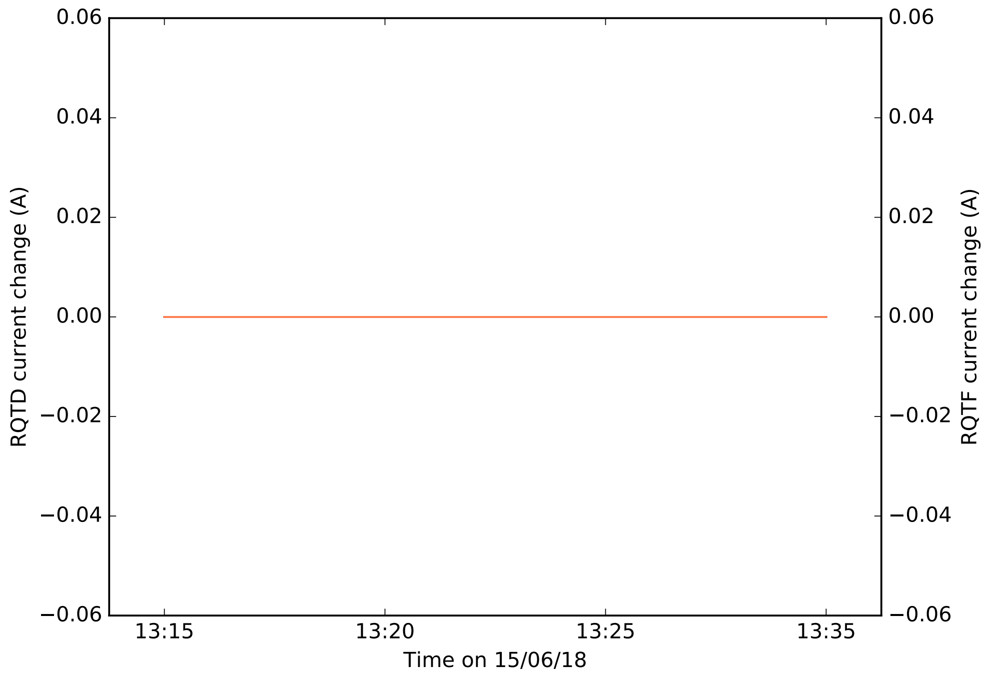

Figure 25: The graph shows the currents flowing through 8 RQTF and 8 RQTD optical correctors between the times 13:15 and 13:35. Since the current did not change in any of the quadrupoles, all 16 plots remain at 0 over the time period.

10.8 Chromaticity

Another possible source of tune jitter is chromaticity. Since the orbit changes, the particle energy changes so we can use Eq. 39 to calculate the tune change from energy shift and chromaticity for the orbit jump from 13:27:26 to 13:27:32. It is reproduced here as:

$$\Delta Q = Q' \frac{dp}{p} = Q' \frac{\langle dx \rangle}{\langle D_x \rangle} \ ,$$

where $\langle dx \rangle$ is the average sextupole horizontal misalignment or the average horizontal orbit jump. From Figure 20, which shows the ring-average horizontal orbit, it can be seen that the orbit jump, $\langle dx \rangle$, is 5.57 μm. The average dispersion, $\langle D_x \rangle$, can be found in the Twiss file generated by the MADX script used to measure certain beam variables for the dataset A time frame for beam 1 as discussed in section 10.3. The variable `DX` [50] was extracted from the Twiss file for every element around the accelerator and the average of these values was calculated to be 1.41 m. The horizontal chromaticity, Q', could similarly be extracted from the MADX generated Twiss file under the variable name `DQ1` [50] and had the value 2.

With these values substituted into Eq. 39 the tune shift from chromaticity was calculated to be

ΔQ = -7.9 $\times$ 10^{-6}. This value is too small to explain the difference in the tune jitter amplitudes so chromaticity cannot be a major alternate source affecting the tune. It could potentially be one source having a very small effect but is most likely a negligible factor. More research would have to be conducted to find the other sources affecting the tune jitters.

10.9 Orbit Feedback System

Since we know that the orbit jump had some effect on the the tunes, it is therefore important that the jump be studied further to identify what caused it so it can be controlled.

The first sources that were looked into to understand the orbit jitters better were sources that could try to change the orbit on purpose. The feedback system tries to kick the orbit back to a reference orbit by changing the current in dipole magnets. Often, this reference orbit used is manually changed to make the new reference orbit fit another path. However, no data for the reference orbit was recorded during the dataset A time frame so this could not be a reason for the large orbit displacement in this case.

The feedback system status was extracted from PyTimber and it was found that it was only switched on for 6 seconds during the time between 13:27:26 and 13:27:32. This can be seen in Figure 26.

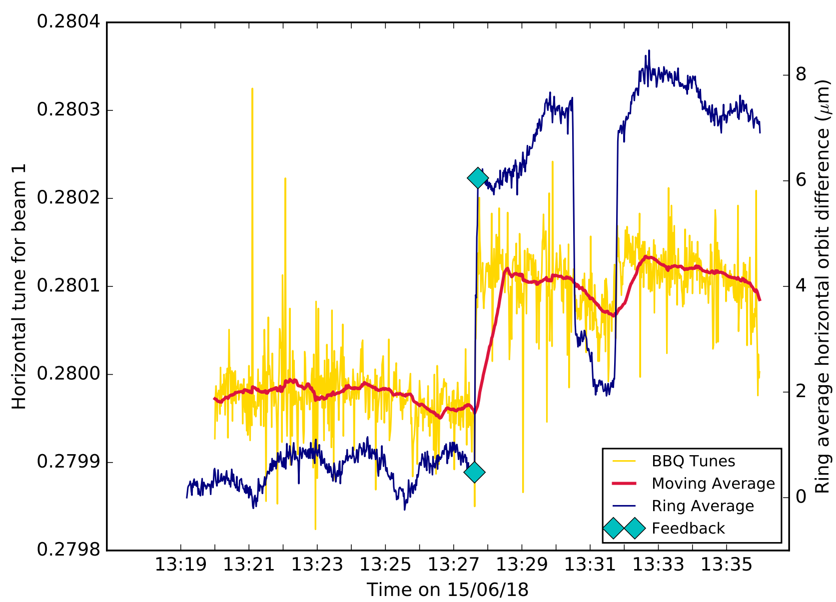

Figure 26: This graph shows the ring average orbit and the measured and moving average tunes in the horizontal direction for beam 1 over a focused time period of 13:09:00 to 13:35:49. The turning on and off of the orbit feedback system is marked at the times 13:27:26 and 13:27:32.

The times at which the orbit feedback was switched on were the exact times of the orbit and tune jump. This strongly suggests that the feedback system being turned on was the reason for the orbit jump. To provide more evidence to this reasoning, the orbit corrector magnets that should have their currents changed by the feedback system were looked into to confirm that they were indeed changing at the time the feedback system was turned on.

10.10 Orbit Correctors

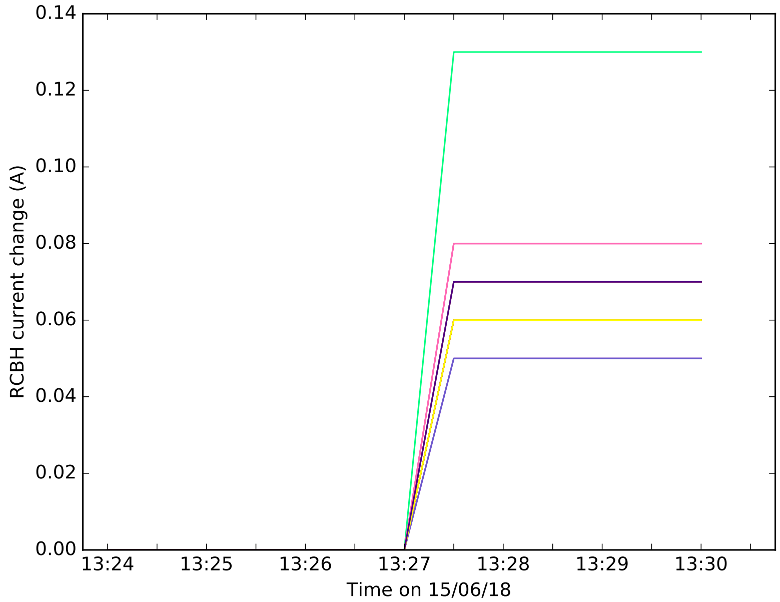

(a) This graphs shows the change in current over a 6 minute period from 13:24 to 13:30.

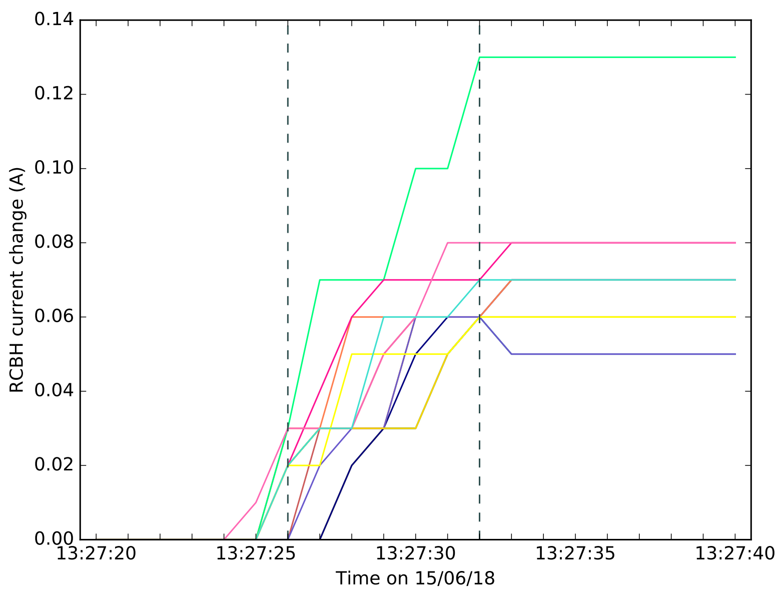

(b) This graph shows the change in current over a 20 second time period of 13:27:20 to 13:27:40. The times at which the orbit feedback system is turned on and off are marked by the dark grey vertical lines.

Figure 27: The graphs above show the change in current over different time periods for 14 orbit corrector magnets that were selected if they underwent a total current change greater than 0.05 A.

In order to see if the feedback system did indeed change the current in orbit correctors to correct the magnet, the currents going through the RCB orbit correctors were inspected. Since only the horizontal orbit is being looked at, the RCB magnets chosen were the horizontal RCBH orbit correctors. For the dataset A time period the magnets did not change until 13:27:27. The majority of the currents flowing through the magnets only changed by 0.01 - 0.05 A. The magnets with the greatest changes in current were selected and these were plotted over the time period 13:24 to 13:30. In order to see the exact changes happening in the current, a graph that focused on the times between 13:27:20 and 13:27:40 was also plotted. The selected magnets are listed in Appendix B.

In both figures, the current changes for 14 orbit corrector magnets are plotted. In Figure 27a only 4 plots are visible but this is because all the current changes occurred between 13:27 and 13:28 and several orbit correctors experienced the same total current change. Figure 27b shows the change in current over a much smaller time frame of 20 seconds from 13:27:20 to 13:27:40. Here it can be seen that the current is only changing at all for 10 seconds between 13:27:23 to 13:27:33, with the greatest current changes occurring in the window that the feedback system is on. Therefore, it can be said that the orbit jump occurred due to the feedback system being turned on and causing the orbit correctors to change the orbit.

11 Conclusions and Further Study

The focus of this thesis was to investigate possible sources of tune jitter so that methods to control them could be developed for the HiLumi LHC. For a selected dataset, the tunes and orbit were extracted and analysed so it could be seen that an orbit jump occurred at the exact same time as a jump in the tunes. The effect of feed-down was examined in order to see if orbit offsets at sextupoles were the primary cause of this large tune jitter. The expected tune shifts from this orbit were calculated using two different methods to increase our confidence in the results. This showed us that the expected tune shift from the observed orbit jump was much larger than the tune jump that was measured for the dataset, so it was concluded that while the orbit at main sextupoles had some effect on the tune jitter it was not the lone source.

The reason as to why the orbit jump occurred in the first place was investigated. It was found that the most likely reason for this orbit jump was because of the orbit feedback system being turned on at the exact time of the jump. During optics measurements with AC dipole kicks, orbit feedback should not be used. There was also, however, an AC dipole kick observed at the exact same time at the tune and orbit jump. It is possible that the AC dipole excitation distorted the orbit feedback. This proves to us that the LHC is an incredibly complex machine and any seemingly inconsequential changes, such as turning on the Orbit Feedback System for just 6 seconds, can have critical impacts on the tune. Explanations as to why the feedback system was turned on could continue to be sought to find ways to control this error source in the future.

Although we can say with a good degree of confidence where the orbit jitters that had some impact on the tune came from, we cannot yet fully explain the difference in expected and observed tune shift from the orbit jump. Within this dataset, there were other observations that could have been looked into further to determine whether they could be a source of tune jitter. The beam 2 horizontal and vertical tunes showed a tune jump larger than that of the beam 1 horizontal and showed a corresponding orbit jump in the RMS orbit. Since this jump happened at the same time as beam 1, it is likely that the jump was also caused by the feedback system, however the orbit correctors for beam 2 should be looked at to confirm this was the reason. We had seen that the beam 1 average horizontal orbit showed a jump at the same time as the tune jump. However we also saw the orbit jumping down and up by a similar amount with no similar correlation in the tunes. An interesting area to explore would be when the orbit jump does affect the tunes and when it does not.

Since the observed tune jitters have smaller amplitudes than predictions from lattice sextupoles, one could make the suggestion that unknown sextupolar errors had a role to play. The data for MCS sextupoles, which are spool-piece corrector magnets that are placed at the end of dipoles to correct the impact of linear chromaticity [48] could also be looked at to examine their effect on the tune. Sextupolar errors, especially in the interaction regions, should be looked into further so that their complete effects on the tune can be known. When particle beams enter detector areas, they are squeezed by insertion magnets so that they collide with particles from the other beam at a higher rate. Three quadrupoles, which make up the inner triplet, are used to make the beam 12.5 times narrower. Since the beta function goes through severe changes during the insertion region period, it would be useful to explore the relationship between the insertion magnets and the tune to see if this could be a reason for tune jumps. Some magnet errors are unavoidable as there will always be additional magnetic field components form the imperfections in the physical magnets [51].

In fact, there are many factors that could affect the tune causing jitters. Since the accelerator is so complex, all changes happening in the machine could potentially have indirect effects on the tune. One way to make the process of managing and controlling these factors easier is to develop a GUI based on Timber that could show the user which magnets and correctors are changing and which systems (such as Orbit Feedback) are turned on and when. This could return information to a beam physicist quickly so that the analysis of tune jitter sources is simpler and more thorough.

By ensuring a higher level of control over these factors, especially over those causing orbit displacements, feed-down effects are less likely. By controlling these factors, the accuracy of β^* measurements can be increased, leading to higher levels of control over luminosity, which is critical for the mission of the HL-LHC to discover new physics.

Appendices

A Timber Variable Names

Timber Variable Name	Units	Description
LHC.BOFSU:EIGEN_FREQ_1_B1	–	Horizontal Tunes Beam 1
LHC.BOFSU:EIGEN_FREQ_2_B1	–	Vertical Tunes Beam 1
LHC.BOFSU:EIGEN_FREQ_1_B2	–	Horizontal Tunes Beam 2
LHC.BOFSU:EIGEN_FREQ_2_B2	–	Vertical Tunes Beam 2
LHC.BOFSU:POSITIONS_H	μm	Horizontal Orbit Positions
LHC.BOFSU:POSITIONS_V	μm	Vertical Orbit Positions
LHC.BOFSU:BPM_NAMES_H	–	Horizontal BPM Names
LHC.BOFSU:BPM_NAMES_V	–	Vertical BPM Names
LHC.BOFSU:ORBIT_FB_STATE	0=OFF, 1=ON	Feedback System State
[magnet name]*:I_MEAS	A	Current through selected magnet

Table 4: This table shows the variables names needed to find the data from PyTimber.
* replace [magnet name] with the name of a corrector magnet from Appendix B.

B Magnets Used in Data

The following is a list of the selected magnets used in section 10.10 and in section 10.7.

B.1 RCB Corrector Magnets

These are the corrector magnets used in Figure 27:

- RPLA.14L2.RCBH13.L2B1
- RPLA.16L6.RCBH15.L6B1
- RPLA.16R6.RCBH16.R6B1
- RPLA.16R8.RCBH16.R8B1
- RPLA.20R6.RCBH20.R6B1
- RPLA.22R6.RCBH22.R6B1
- RPLA.26L5.RCBH26.L5B1
- RPLA.26R4.RCBH26.R4B1
- RPLA.28L5.RCBH28.L5B1
- RPLA.28L8.RCBH27.L8B1

- RPLA.28R3.RCBH27.R3B1
- RPLA.30L5.RCBH30.L5B1
- RPLA.32L2.RCBH31.L2B1
- RPLA.32L5.RCBH32.L5B1

B.2 RQT Focusing Optical Correctors

These are the focusing optical correctors used in Figure 25:

- RPMBB.UA23.RQTF.A12B1
- RPMBB.UA27.RQTF.A23B1
- RPMBB.UA43.RQTF.A34B1
- RPMBB.UA47.RQTF.A45B1
- RPMBB.UA63.RQTF.A56B1
- RPMBB.UA67.RQTF.A67B1
- RPMBB.UA83.RQTF.A78B1
- RPMBB.UA87.RQTF.A81B1

B.3 RQT Defocusing Optical Correctors

These are the defocusing optical correctors used in Figure 25:

- RPMBB.UA23.RQTD.A12B1
- RPMBB.UA27.RQTD.A23B1
- RPMBB.UA43.RQTD.A34B1
- RPMBB.UA47.RQTD.A45B1
- RPMBB.UA63.RQTD.A56B1
- RPMBB.UA67.RQTD.A67B1:
- RPMBB.UA83.RQTD.A78B1
- RPMBB.UA87.RQTD.A81B1

References

[1] T. Persson et al. "LHC optics commissioning: A journey towards 1% optics control". In: Phys. Rev. Accel. Beams 20, 061002 (2017).

[2] D.W. Wolf. "Analysis of Tune Modulations". In: CERN-THESIS-2018-251 ; ETP-Bachelor-KA/2018-22 (2018).

[3] CERN. *About CERN*. URL: `https://home.cern/about`. (accessed: 30.06.19).

[4] L. Di Lella and C. Rubbia. *The Discovery of the W and Z Particles*. 2015. URL: `https://cds.cern.ch/record/2103277/files/9789814644150_0006.pdf`.

[5] CERN. *First atoms of antimatter produced at CERN*. 1996. URL: `https://home.cern/news/press-release/cern/first-atoms-antimatter-produced-cern`. (accessed: 30.06.19).

[6] The ATLAS Collaboration. "Observation of a new particle in the search for the Standard Model Higgs boson with the ATLAS detector at the LHC". In: CERN-PH-EP-2012-218 (2012).

[7] CERN. *The accelerator complex*. URL: `https://home.cern/science/accelerators/accelerator-complex`. (accessed: 30.06.19).

[8] J. Gillies. *Luminosity? Why don't we just say collision rate?* 2011. URL: `https://home.cern/news/opinion/cern/luminosity-why-dont-we-just-say-collision-rate`. (accessed: 31.06.19).

[9] C. Pralavorio. *Record luminosity: well done LHC*. 2017. URL: `https://home.cern/news/news/accelerators/record-luminosity-well-done-lhc`. (accessed: 30.06.19).

[10] CERN. *The HL-LHC Project*. URL: `http://hilumilhc.web.cern.ch/`. (accessed: 30.06.19).

[11] CERN. *Future Circular Collider*. URL: `https://home.cern/science/accelerators/future-circular-collider`. (accessed: 30.06.19).

[12] W. Herr and B. Muratori. *Concept of luminosity*. 2003. URL: `https://cds.cern.ch/record/941318/files/p361.pdf`.

[13] CERN. *X. C. Vidal and R. C. Manzano*. URL: `https://www.lhc-closer.es/taking_a_closer_look_at_lhc/0.cross_section`. (accessed: 30.06.19).

[14] K. Potter. *Luminosity Measurements and Calculations*. 2018. URL: `https://userweb.jlab.org/~parkkj/USC/proposal2009/local_disk/MEIC/lumi_collider.pdf`.

[15] F. Carlier et al. "Accuracy and feasibility of the beta* measurement for LHC and High Luminosity LHC using k-modulation". In: Phys. Rev. Accel. Beams, 20, 011005 (2017).

[16] A. Latina. *Effects of Element Misalignments on Accelerator Performance*. PowerPoint. URL: `https://indico.cern.ch/event/458671/contributions/2187799/attachments/1289619/1920127/Presentation.pdf`. (accessed: 30.06.2019).

[17] O. Bruning. "Intermediate Course on Accelerator Physics: Linear Imperfections". In: CERN-2006-002 (2006), pp. 129–180.

[18] J. Rossbach and P. Schmuser. "Basic Course on Accelerator Optics". In: DESY-M-93-02 (1993).

[19] M. Martini. "An Introduction to Transverse Beam Dynamics in Accelerators". In: CERN/PS 96-11 (PA) (1996).

[20] M. J. Ward. *UBC Math Department: Basic Floquet Theory*. URL: `http://www.math.ubc.ca/~ward/teaching/m605/every2_floquet1.pdf`. (accessed: 30.06.19).

[21] Y. Papaphilippou. *Linear Imperfections and Correction*. PowerPoint. URL: `https://yannis.web.cern.ch/yannis/teaching/juaslinearimperfections.pdf`. (accessed: 30.06.2019).

[22] S. Giuducci. "Chromaticity". In: CERN-94-01-Vol. 1 (1994). URL: `https://cds.cern.ch/record/398300/files/p191.pdf`. (accessed: 30.06.2019).

[23] E. J. N. Wilson. *Intermediate Course on Accelerator Physics: Linear Imperfections*. CERN-2006-002. 2006, pp. 1–29.

[24] J. Serrano and M. Cattin. "The LHC AC Dipole system: an introduction". In: CERN-BE-Note-2010-014 (2010).

[25] O. Bruning et al. *LHC Design Report Volume I: The LHC Main Ring*. CERN, 2004, pp. 29–32. URL: `https://cds.cern.ch/record/782076/files/`. (accessed: 30.06.19).

[26] H. Schmickler. "Beam Position Measurement System Design". In: THALA01 (2015).

[27] R. J. Steinhagen. *Large Scale Orbit Correction for the LHC*. PowerPoint. URL: `http://iwbs2004.web.psi.ch/documents/program/Steinhagen.Ralph/1.pdf`. (accessed: 30.06.2019).

[28] O. Bruning. *Intermediate Course on Accelerator Physics: Linear Imperfections*. CERN-2006-002. 2006, pp. 176–180.

[29] J. Koutchouk. "Trajectory and Closed Orbit Correction". In: CERN-LEP-TH-89-2 (1989).

[30] H. Grote, F. Schmidt, and L. Deniau. *The MAD-X Program User's Reference Manual*. Version 5.02.08. CERN, 2016, p. 172. URL: `https://madx.web.cern.ch/madx/`. (accessed: 30.06.19).

[31] *CERN eLogBook*. URL: `https://op-webtools.web.cern.ch/elogbook/index.php`. (accessed: 30.06.19).

[32] S. Fartoukh et al. "Round telescopic optics with large telescopic index". In: CERN-ACC-2018-0032 (2018).

[33] The CMS and TOTEM Collaborations. "CMS-TOTEM Precision Proton Spectrometer Technical Design Report". In: CERN-LHCC-2014-02 (2014).

[34] J. Coello et al. "MD Test of a Ballistic Optics". In: CERN-ACC-NOTE-2016-0008 (2016).

[35] M. Gasior. *3D-BBQ*. URL: `https://mgasior.web.cern.ch/mgasior/pro/bbq/index.html`. (accessed: 30.06.19).

[36] T. Pieloni and B. Salvant. *BBQ System*. PowerPoint. The URL leads to a site where the PowerPoint can be accessed. URL: `https://emetral.web.cern.ch/emetral/ICEsection/2011/2011-03-02/ICE%20Min%20meeting_02-03-11.htm`. (accessed: 30.06.2019).

[37] R. De Maria et al. *Pytimber*. URL: `https://indico.cern.ch/event/560447/attachments/1327595/1993250/PyTimber.pdf`. (accessed: 30.06.19).

[38] Riccardo De Maria. *GitHub - Pytimber*. URL: `https://github.com/rdemaria/pytimber`. (accessed: 30.06.19).

[39] The Python Community. *Python Data Analysis Library*. URL: `https://pandas.pydata.org/`. (accessed: 30.06.19).

[40] J. Wenninger et al. *Orbit Feedback at the LHC*. PowerPoint. URL: `https://indico.cern.ch/event/743699/contributions/3072646/attachments/1749290/2838653/ARIES18.LHCOrbitFB.JW.pdf`. (accessed: 30.06.2019).

[41] J. L. Gonzalez et al. "The Measurement of Bunch Intensity using the LHC BPM System". In: (2009). URL: `https://accelconf.web.cern.ch/accelconf/d09/papers/mopd09.pdf`. (accessed: 30.06.2019).

[42] Python Software Foundation. *Python Documentation - Pickle*. URL: `https://docs.python.org/2.7/library/pickle.html`. (accessed: 30.06.19).

[43] The SciPy Community. *numpy.mean: NumPy v1.16 manual*. URL: `https://docs.scipy.org/doc/numpy/reference/generated/numpy.mean.html`. (accessed: 30.06.19).

[44] The SciPy Community. *numpy.std: NumPy v1.16 manual*. URL: `https://docs.scipy.org/doc/numpy/reference/generated/numpy.std.html`. (accessed: 30.06.19).

[45] The SciPy Community. *scipy.stats.pearsonr: SciPy v0.14.0 Reference Guide*. URL: https://docs.scipy.org/doc/scipy-0.14.0/reference/generated/scipy.stats.pearsonr.html. (accessed: 30.06.19).

[46] H. Grote, F. Schmidt, and L. Deniau. *The MAD-X Program User's Reference Manual*. Version 5.02.08. CERN, 2016, p. 62. URL: https://madx.web.cern.ch/madx/. (accessed: 30.06.19).

[47] J. Vazquez. *CERN OMC Glossary*. 2014. URL: https://twiki.cern.ch/twiki/bin/view/BEABP/Glossary. (accessed: 30.06.19).

[48] O. Bruning et al. *LHC Design Report Volume I: The LHC Main Ring*. CERN, 2004, p. 32. URL: https://cds.cern.ch/record/782076/files/. (accessed: 30.06.19).

[49] T. Persson et al. "Review of the LHC Online Model Implementation and of its applications". In: TUPMW030 (2016).

[50] H. Grote, F. Schmidt, and L. Deniau. *The MAD-X Program User's Reference Manual*. Version 5.02.08. CERN, 2016, pp. 20–21. URL: https://madx.web.cern.ch/madx/. (accessed: 30.06.19).

[51] CERN. *Pulling together: Superconducting electromagnets*. URL: https://home.cern/science/engineering/pulling-together-superconducting-electromagnets. (accessed: 30.06.19).